Submitted

Understanding surface-wave modal content for high-resolution imaging of submarine sediments with Distributed Acoustic Sensing

Loïc Viens[1], Mathieu Perton[2], Zack J. Spica[1], Kiwamu Nishida[3], Masanao Shinohara[3], and Tomoaki Yamada[3]

[1] *Department of Earth and Environmental Sciences, University of Michigan, Ann Arbor, Michigan, USA*

[2] *Instituto de Ingeniería, Universidad Nacional Autónoma de México, CDMX, Mexico*

[3] *Earthquake Research Institute, The University of Tokyo, Tokyo, Japan*

15 April 2022

SUMMARY

Ocean Bottom Distributed Acoustic Sensing (OBDAS) is emerging as a new measurement method providing dense, high-fidelity, and broadband seismic observations from fibre-optic cables deployed offshore. In this study, we focus on 33 km of a telecommunication cable located offshore the Sanriku region, Japan, and apply seismic interferometry to obtain a high-resolution 2-D shear-wave velocity (V_S) model below the cable. We first show that the processing steps applied to two weeks of continuous data prior to computing Cross-Correlation Functions (CCFs) impact the modal content of surface waves. Data pre-processed with 1-bit normalisation allow us to retrieve dispersion images with high Scholte-wave energy between 0.5 and 5 Hz, whereas spatial aliasing dominates dispersion images above 3 Hz for non-1-bit CCFs. Moreover, the number of receiver channels considered to compute dispersion images also greatly affects the resolution of extracted surface-wave modes. In some regions of the array, we observe up to 30 higher modes. To better understand the remarkably rich modal nature of OBDAS data, we simulate Scholte-wave dispersion curves from constant V_S gradient media. For soft marine sediments, simulations confirm that a large number of modes can be generated. Based on pre-processing and theoretical considerations, we extract surface-wave dispersion curves from 1-bit CCFs spanning over 400 channels (i.e., $\sim$2 km) along the array and invert them to image the subsurface. The 2-D velocity profile generally exhibits slow shear-wave velocities near the ocean floor that gradually increase with depth. Lateral variations are also observed. Flat bathymetry regions, where sediments tend to accumulate, reveal a larger number of Scholte-wave modes and lower shallow velocity layers than regions with steeper bathymetry. We also compare and discuss the velocity model with that from a previous study and finally discuss the combined effect of bathymetry and shallow V_S layers on earthquake wavefields. Our results provide new constraints on the shallow submarine structure in the area and further demonstrate the potential of OBDAS for high-resolution offshore geophysical prospecting.

Key words: Scholte waves, Tomography, Japan, surface wave

1 INTRODUCTION

Oceans cover more than 70% of the Earth's surface. However, the offshore Earth's structure remains greatly under-explored due to the high-pressure conditions and high costs involved in deploying seismic instruments on the ocean floor. Real-time offshore seismic arrays, such as DONET and S-net in Japan (Aoi et al. 2020), have recently been installed in highly seismically active regions. While such networks can greatly contribute to earthquake early warning systems by detecting earthquakes seconds earlier than traditional onshore networks, their sensor's density is too low to provide high-resolutions images of the shallow subsurface. In this context, Distributed Acoustic Sensing (DAS) appears as an enticing alternative to take advantage of existing cabled networks and study the physical properties of Earth near the coast with an unprecedented spatial resolution.

DAS is a rapidly evolving technology in geophysics that turns standard optical fibres into seismic arrays measuring the Earth's vibrations over tens of kilometres with a spatial density of the order of the metre. The DAS technology uses an optoelectrical interrogator to probe fibre-optic cables with repeated laser pulses. An interferometer subsequently analyses phase shifts of the back-scattered Rayleigh light along the cable over a sliding spatial distance (i.e., the gauge length). Depending on the manufacturing design, the phase shifts are convert to longitudinal strain or strain-rate time-series along the axis of the cable. For an extensive review of the DAS technology, we refer the reader to Hartog (2017).

Millions of kilometres of fibre-optic cables have been deployed around the world over the past decades to support our modern telecommunication network. Many of these fibres are located off-shore and could therefore compensate for the scarcity of seismic stations deployed on the ocean floor. Ocean-bottom DAS (OBDAS) has recently emerged as a promising method to detect and monitor a multitude of physical marine phenomena. For example, OBDAS has been used to monitor the spatial evolution of near-coast microseisms (Lindsey et al. 2019; Sladen et al. 2019; Spica et al. 2020; Williams et al. 2019), provide high-fidelity records of regional and teleseismic earthquake wavefields (Lior et al. 2021; Shinohara et al. 2019; Spica et al. 2022), detect T-phases and other acoustic waves (Rivet et al. 2021; Ugalde et al. 2021; Spica et al. 2022), and track ocean surface gravity waves and deep-ocean water mixing processes (Ide et al. 2021).

OBDAS measurements also offer new possibilities for imaging marine sediments at a spatial resolution and an extent previously unattainable with traditional passive seismic surveys (Cheng et al. 2021; Lior et al. 2022; Spica et al. 2020, 2022; Tonegawa et al. 2022; Williams et al. 2021). Moreover, Karrenbach et al. (2020) and Matsumoto et al. (2021) demonstrated that OBDAS can record active source shots with a fidelity similar to that of ocean-bottom seismometers. The success of these early studies can be attributed to the fact that travel-time based analysis, using earthquakes or the ambient seismic field (ASF), should theoretically yield the same result for both DAS and geophone-equivalent data (Nayak et al. 2021; Wang et al. 2018; Zeng et al. 2017). Therefore, traditional imaging techniques are readily applicable to the OBDAS datasets; although they need to be adapted to the exceptional spatial sampling of OBDAS data.

Seismic interferometry is a well established method to extract the seismic wave propagation between two sensors. Under certain conditions, cross-correlating ASF time series recorded at two seismometers yields the elastodynamic response of the Earth between these stations (e.g., Shapiro & Campillo 2004). The surface-wave component of the Cross-Correlations Functions (CCFs) is generally better retrieved as the ASF sources mostly generate surface waves and seismometers are located on the Earth's surface (e.g., Spica et al. 2017). The dispersive properties of surface waves from CCFs have been extensively used to image the crust and the uppermost mantle worldwide (Castellanos et al. 2018; Lin et al. 2007; Nishida et al. 2008; Sabra et al. 2005; Spica et al. 2016; Stehly et al. 2009; Yao et al. 2006). During the last decade, dense offshore arrays have been deployed for seismic exploration purposes and ASF tomography has been applied to obtain high-resolution images of the submarine shallow structure (Bussat & Kugler 2011; de Ridder & Dellinger 2011; Mordret et al. 2013, 2014). While very successful, these studies primarily focused on the fundamental and first-higher modes of surface waves. Nevertheless, retrieving higher-order surface-wave modes in marine environments could greatly enhance the resolution of these models and better constrain the deeper structure (e.g., Aki & Richards 2002; Perton et al. 2019; Socco & Strobbia 2004).

In this study, we retrieve multi-mode Scholte waves from the ASF recorded along a fibre-optic cable located offshore the Sanriku coast, Japan, using seismic interferometry. We first discuss the effect of data preprocessing on the retrieval of accurate dispersion images and perform numerical simulations to better understand the nature of the large number of surface-wave modes (over 30 modes in some sections of the cable). Based on data processing and theoretical considerations, we then perform a multi-mode inversion to constrain the shallow shear-wave velocity (V_S) structure along the cable. Finally, we investigate the stability of the results, compare the inverted 2-D model with that from a previous study, and discuss the impact of the subsurface on earthquake wavefields.

2 DATA

2.1 The Kamaishi cable

A 120-km long submarine cable offshore the Sanriku coast was installed in 1996 to record real-time data from an ocean-bottom observatory composed of three ocean-bottom accelerometers and two pressure gauges (Figure 1, Kanazawa & Hasegawa 1997; Shinohara et al. 2021, 2022). An

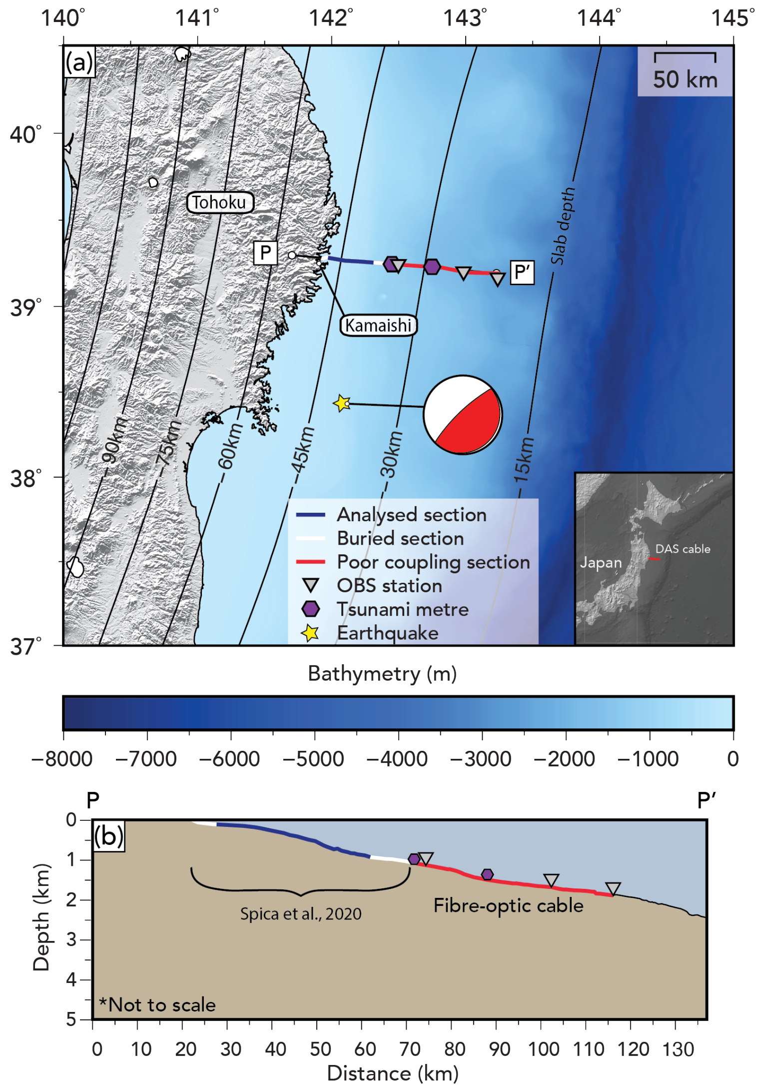

Figure 1. (a) Map showing the location of the fibre-optic cable offshore Japan. The fibre sustains three ocean-bottom accelerometers (inverted triangles) and two pressure gauges (purple hexagons). The blue section of the cable highlights the section analysed in this study between channels 1500 to 8500. The white and red sections of the cable depict areas where the fibre is buried and where it lays on the ocean floor by gravity, respectively. The subvertical solid lines depict the subducting slab iso-depths (Hayes et al. 2018). The location of a M_w 3.7 earthquake discussed in Figure 10 is highlighted by a star and its moment tensor. The inset map shows the Japanese Islands and the location of the cable in red. (b) Bathymetry profile along P-P' shown in (a). The location of the tomography performed by Spica et al. (2020) is also indicated.

s

AP Sensing N5200A interrogator unit with a 70-km sensing range (Cedilnik et al. 2019) was used to record strain data with a 500 Hz sampling rate from November 18 to December 2, 2019. The gauge length was set to 40 m and the spatial sampling to 5.1 m. The first 47.7 km of the cable from the landing station (i.e., the first ∼9350 channels) are buried under 60–70 cm of sediments below the ocean floor. The channel positions were recently precisely located using active sources (Takano et al. 2021) and we focus on the data recorded between channel numbers 1500 and 8500, corresponding to 7.65 km and 43.35 km from the coast, respectively. The analysed section of the cable is relatively straight and the buried cable guaranties a good coupling with the sediments. More details about the cable setup and measurement quality can be found in Shinohara et al. (2019) and Spica et al. (2020).

3 METHODS

3.1 Cross-correlation functions and dispersion curves

For each channel, the two-week dataset is windowed into 20-min time series, detrended, demeaned, filtered between 0.01 and 5 Hz (a four-pole two-pass Butterworth filter is used for all filtering operations), and down-sampled to 10 Hz. We also process the data with and without 1-bit normalisation (Bensen et al. 2007) to investigate the impact of this non-linear operation on the retrieval surface-wave higher modes. We set up virtual sources every 10 channels (i.e., every 51 m) between channels 1500 and 8000 and compute CCFs with the following 500 channels from each virtual source (i.e., channels 2000 to 2500 for virtual source 2000). For each station pair, the CCFs are computed for each 20-min window in the frequency domain as

$$\mathrm{CCF}_{v-r}(t) = \mathfrak{F}^{-1}\left(\frac{\hat{s}_v \hat{s}_r^*}{\{|\hat{s}_v|\}\{|\hat{s}_r|\}}\right), \quad (1)$$

where $\hat{s}_v$ and $\hat{s}_r$ are the Fourier transform of 20-min strain records at the virtual source (s_v) and the receiver channel (s_r), respectively. The $*$ symbol represents the complex conjugate. Spectral whitening is applied and is represented by the denominator term of Equation 1 (e.g., $\{|\hat{s}_v|\}\{|\hat{s}_r|\}$), where $\{\cdot\}$ represents a smoothing of the absolute amplitude spectrum ($|\cdot|$) using a running-mean average algorithm over 30 samples (Bensen et al. 2007). The inverse Fourier transform ($\mathfrak{F}^{-1}$) is finally applied to retrieve the 20-min CCFs in the time domain.

For each channel pair, we stack 934 20-min CCFs calculated over the two-week dataset using the Phase-Weighed Stack method (Schimmel & Paulssen 1997) with a power of 2 and a smoothing

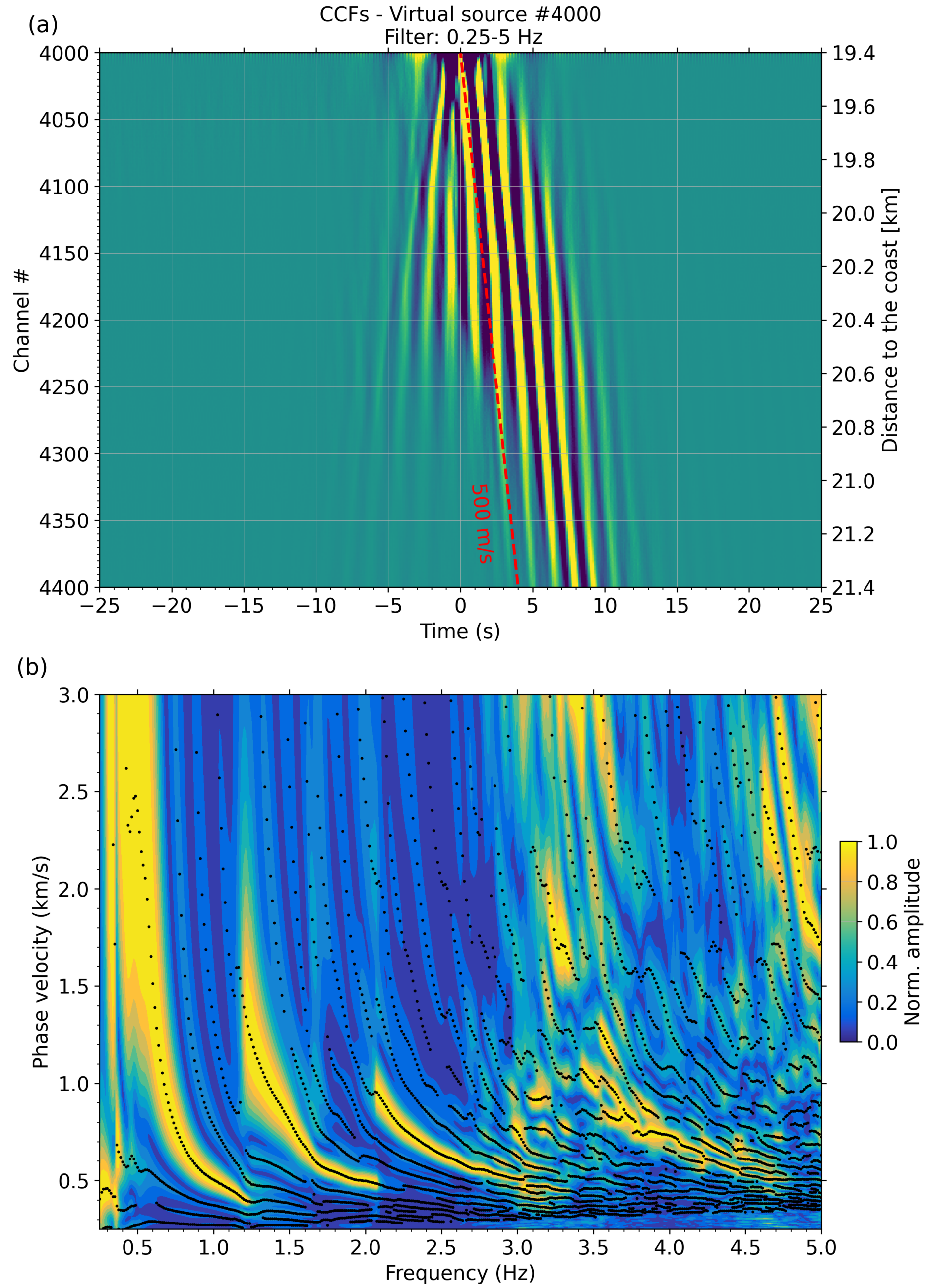

Figure 2. (a) CCFs computed with 1-bit normalisation between the virtual source 4000 and channel 4400. The dashed red line highlights the 500 m/s phase velocity moveout. All the waveforms are bandpass filtered between 0.25 and 5 Hz. (b) Dispersion image obtained from the causal part of the CCFs shown in (a). The black dots show the selected phase velocity dispersion points used to perform the inversion.

of 5. The stacked CCFs are finally filtered between 0.25 and 5 Hz to remove the contribution of ocean surface gravity waves, which dominate the CCFs at frequencies below 0.25 Hz (Spica et al. 2020). In Figure 2a, we show an example of the CCFs calculated with 1-bit normalisation between the virtual source 4000 and channel 4400. The CCFs are computed between strain data measured along the axis of the cable and are therefore mostly sensitive to surface waves travelling longitudinally to the fibre (e.g., Rayleigh and Scholte waves, Martin et al. 2021). Clear propagating Scholte waves can be observed in both the anti-causal (negative) and causal (positive) parts of the CCFs. In this study, we only analyse the causal part of the CCFs (e.g., oceanward propagation), which has a stronger signal-to-noise ratio.

We use a frequency-domain slant-stack method to compute dispersion images from CCFs (Park et al. 1998). A Fourier transform is first applied to the causal part of the time domain CCFs to retrieve the corresponding frequency-offset domain representation. Then, a slant-stack algorithm is used to retrieve the phase dispersion spectrum. In Figure 2b, we show the dispersion image computed from the 1-bit CCFs displayed in Figure 2a. Multiple dispersive features can be observed for this section of the cable between 0.5 and 5 Hz.

Most ambient noise tomography studies primarily focus on the surface-wave fundamental mode, which is assumed to be the most energetic and to exhibit a global maximum at each frequency. In this study, dispersion images are exceptionally rich in high-energy higher modes. To take advantage of all possible modes and to avoid incorrect mode assignments, we follow the method proposed by Spica et al. (2018) and select the local maximum energy at all frequencies, rather than the global maximum energy (Figure 2b). While most selected points can be directly related to dispersive features, some are potential artefacts. In Sections 3.2.1 and 3.3, we further discuss the nature of such artefacts and present a way to refine and improve the picking process of dispersion points.

3.2 Data processing considerations

3.2.1 On the effect of 1-bit normalisation

Pre-processing DAS data with 1-bit normalisation prior to computing CCFs is critical for retrieving dispersion curves (DCs) at high frequencies. In Figure 3, we show the causal part of the CCFs computed with and without 1-bit normalisation between virtual source 4000 and channel 4400, as well as their respective dispersion images. In the time domain, CCFs computed with 1-bit

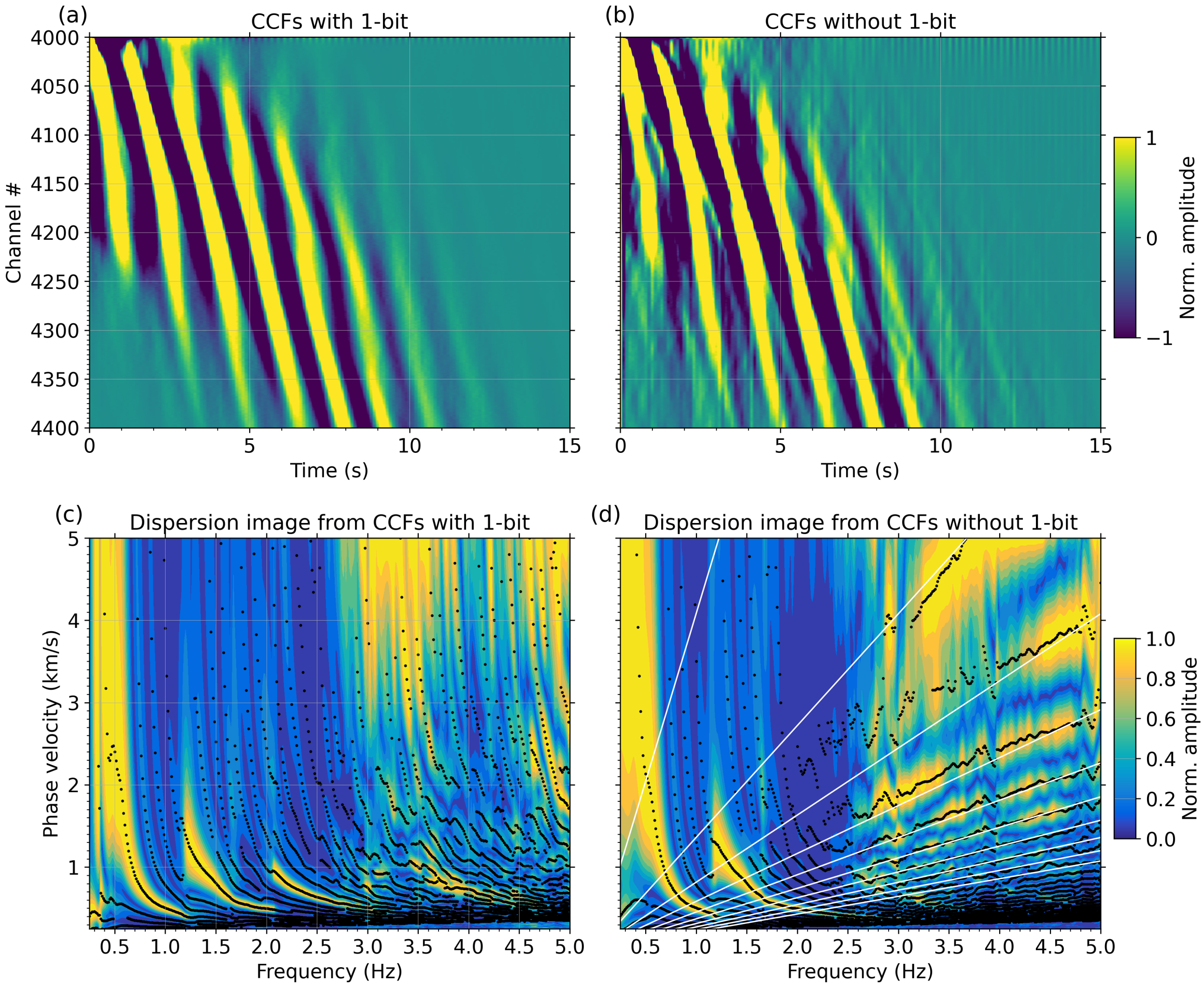

Figure 3. CCFs computed (a) with and (b) without 1-bit normalisation between virtual source 4000 and channel 4400. All the waveforms are filtered between 0.25 and 5 Hz. (c) Dispersion image obtained from the CCFs shown in (a) together with the selected phase dispersion points (black dots). (d) Same as (c) for the CCFs shown in (b). The white lines depicts the first 10 spatial aliasing lines (i.e., $i = 10$, Equation 2).

normalisation exhibit clearer propagating seismic waves than those computed without it (Figures 3a-3b). The respective dispersion images and the extracted dispersion points are very similar for frequencies below 2 Hz, but clear differences can be observed at higher frequencies (Figures 3c-3d). The dispersion image obtained from non-1-bit CCFs exhibits high-energy straight lines that increase with increasing frequency (Figure 3d). These lines are caused by spatial aliasing and appear at high frequency where the incoherent noise energy is stronger than the surface-wave energy. In this study, spatial aliasing obeys the relationship

$$c_i = \frac{\Delta x \times n_s}{0.5 + i} \times f, \tag{2}$$

where c, Δx, n_s, and f are the phase velocity, channel spacing (i.e., 5.1 m), number of channels used in the slant-stack analysis (i.e., array aperture), and frequency, respectively. i is a positive integer that defines the slope of spatial aliasing lines. Equation 2 is very similar to that from Dai et al. (2018, their Equation 7), except that the slope of spatial aliasing lines depends on the array aperture used in the slant-stack analysis (Figure S1). Nevertheless, 1-bit normalisation generally allows us to retrieve higher modes with significant energy at high frequencies and reduce the effect of spatial aliasing.

3.2.2 On the effect of the number of receivers

The number of receivers used in the slant-stack analysis impacts the spectral resolution of dispersion images. More specifically, surface-wave modes cannot be properly separated if the array aperture is too small (Foti et al. 2015). In Figure 4, we show the dispersion images computed from 1-bit CCFs by considering 200, 300, 400, and 500 receivers, which corresponds to array apertures of 1020, 1530, 2040, and 2550 m, respectively. Note that we change the virtual source location to ensure that the middle point of each set of CCFs remains the same (e.g., channel 3000 in Figure 4). The resolution of dispersion images and the number of DCs significantly increase with respect to the number of receivers. For 200 channels, four coarse modes appear between 0.5 and 5 Hz. By broadening the array aperture, we are able to better separate higher modes and retrieve sharper dispersive features with many local maxima up to 5 Hz.

In Figure 4b, we show the selected dispersion points for 300, 400, and 500 receivers. For velocities faster than 1 km/s, we observe that the modal content slightly increases between 300 and 400 receiver channels, but remains almost stable between 400 and 500 channels. This suggests that we converge toward a reliable representation of the deep structure, which generally exhibits less lateral variations than shallow layers. For velocities slower than 1 km/s, the broadening of the array aperture from 300 to 500 channels increases the modal content, but comes at a cost of

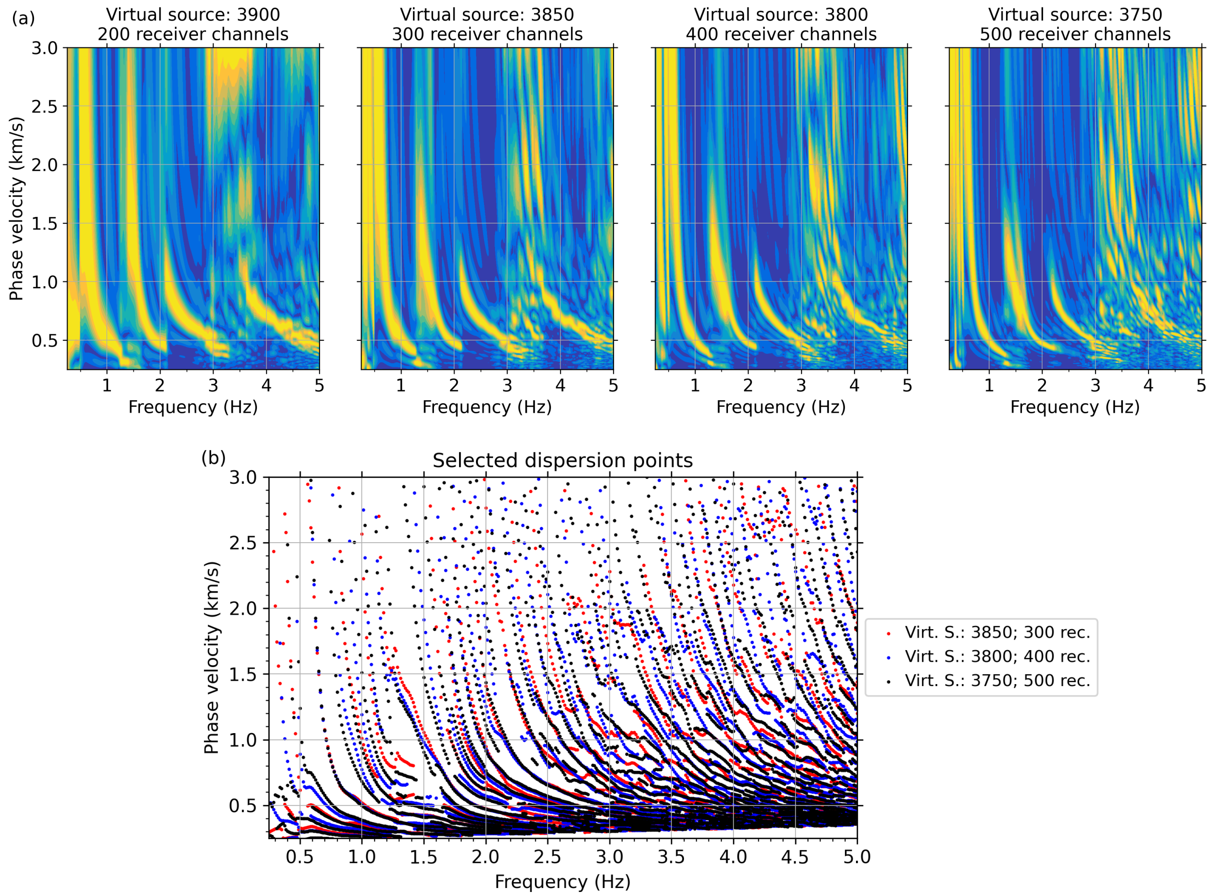

Figure 4. (a) Dispersion images computed from 1-bit CCFs by considering 200, 300, 400, and 500 receivers. The virtual source is shifted so that DCs focus on the same medium. (b) Selected dispersion points computed from the panels in (a) for 300, 400, and 500 receivers.

smoothing potential lateral velocity variations (Foti et al. 2015). Therefore, we select 400 receivers as a trade-off between mode separation and lateral resolution.

3.3 On the variability of dispersion images along the array

Based on the analysis performed in Section 3.2, we compute dispersion images from 1-bit CCFs over 400 receivers. In Figure 5, we show a subset of dispersion images computed at 14 different positions along the cable. We observe significant differences between the dispersion images, especially in terms of modal content. Between channels 1500 and 4000, the modal content is particularly rich. However, spatial aliasing appears after virtual source 4500 and even dominates at virtual source 5500 despite the fact that CCFs are computed with 1-bit normalisation. Yet, clear

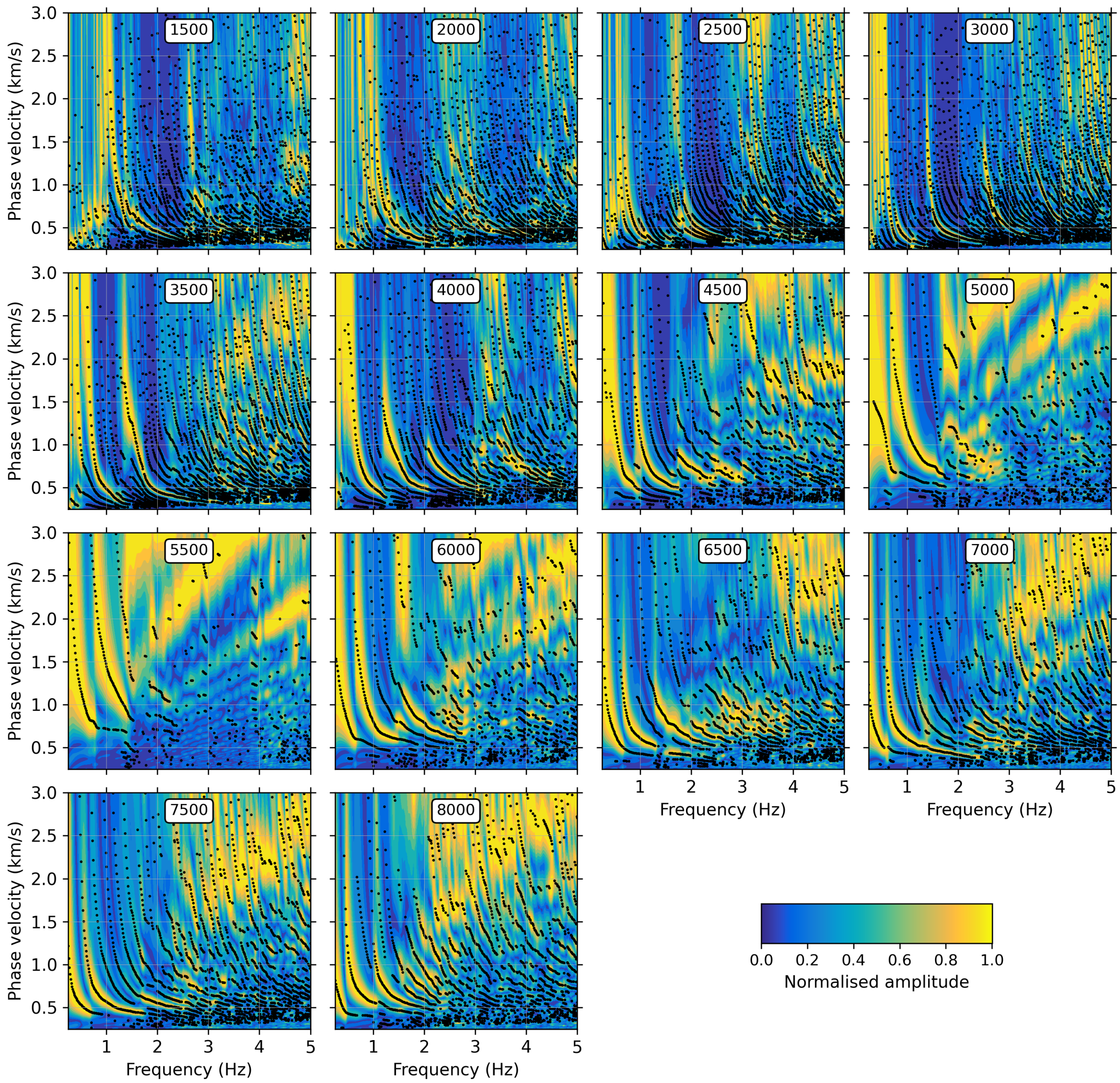

Figure 5. Dispersion images computed from 1-bit CCFs and by considering 400 receivers along the cable; every 500 virtual sources. Selected dispersion points, after rejecting spatial aliasing artefacts, are shown by the black dots.

modes can still be observed below 1.5 Hz between virtual sources 4500 and 5500. We further discuss the lateral variations of the dispersion image modal content in Section 4.2.

High energy artefacts caused by spatial aliasing need to be removed from the selected local maximum energy points, as they can bias the inversion results. We reject selected points that increase with both velocity and frequency and show the effect of the selection process in Figure S2 at three virtual sources. In Figure 5, we only show the selected dispersion points used to perform the inversion. Note that some selected dispersion points appear at some specific frequencies in dispersion images where spatial aliasing is present (i.e., near 4.8 Hz for virtual source 5500), and are used to better constrain the inversion. Nevertheless, further analysis beyond the scope of this study is needed to better understand this phenomenon.

3.4 Theoretical considerations: constant V_S gradients and modal content

Two types of waves can propagate along a flat solid-fluid interface: Leaky-Rayleigh and Scholte waves (Gusev et al. 1996; Zhu et al. 2004). The term 'leaky' is used as Rayleigh waves radiate energy not only in the solid but also in the fluid, which causes their fast attenuation with distance. For a hard solid medium (e.g., V_S in the solid is much higher than the acoustic fluid velocity), most of the energy is lost in leaky-Rayleigh waves and the penetration of Scholte waves is limited to solid media presenting a gradient velocity (Glorieux et al. 2001). However, for a medium where V_S is much slower than the acoustic fluid velocity, leaky-Rayleigh waves disappear and Scholte waves can be used to accurately assess V_S in the solid (Ali & Broadhead 1995). Sedimentary media, and more particularly marine sediments, are composed of soft materials which generally present a V_S gradient with depth and a near-null velocity at the top interface (Hamilton 1979). The effect of gradient media on the propagation of body waves has been finely studied in refraction seismology and body-wave travel-time studies (e.g., Stein & Wysession 2003). Yet, its effect on surface-wave propagation is not as well constrained, especially in marine environments.

We present a simple theoretical case to illustrate the effect of constant V_S gradient media on the propagation of surface waves. While the nature of the subsurface generally differs from a constant velocity gradient, simulations can helps us to better understand DAS observations and validate the approach that we propose. As we only consider media with very slow shear-wave velocities, we perform the simulations with a layered solid half-space medium without a water layer. Nevertheless, we numerically confirm that the computed DCs are identical to those obtained with a solid half-space medium overlaid by a water layer, but have a higher computational stability. This demonstrates that leaky-Rayleigh waves are not excited in the media considered for the simulations.

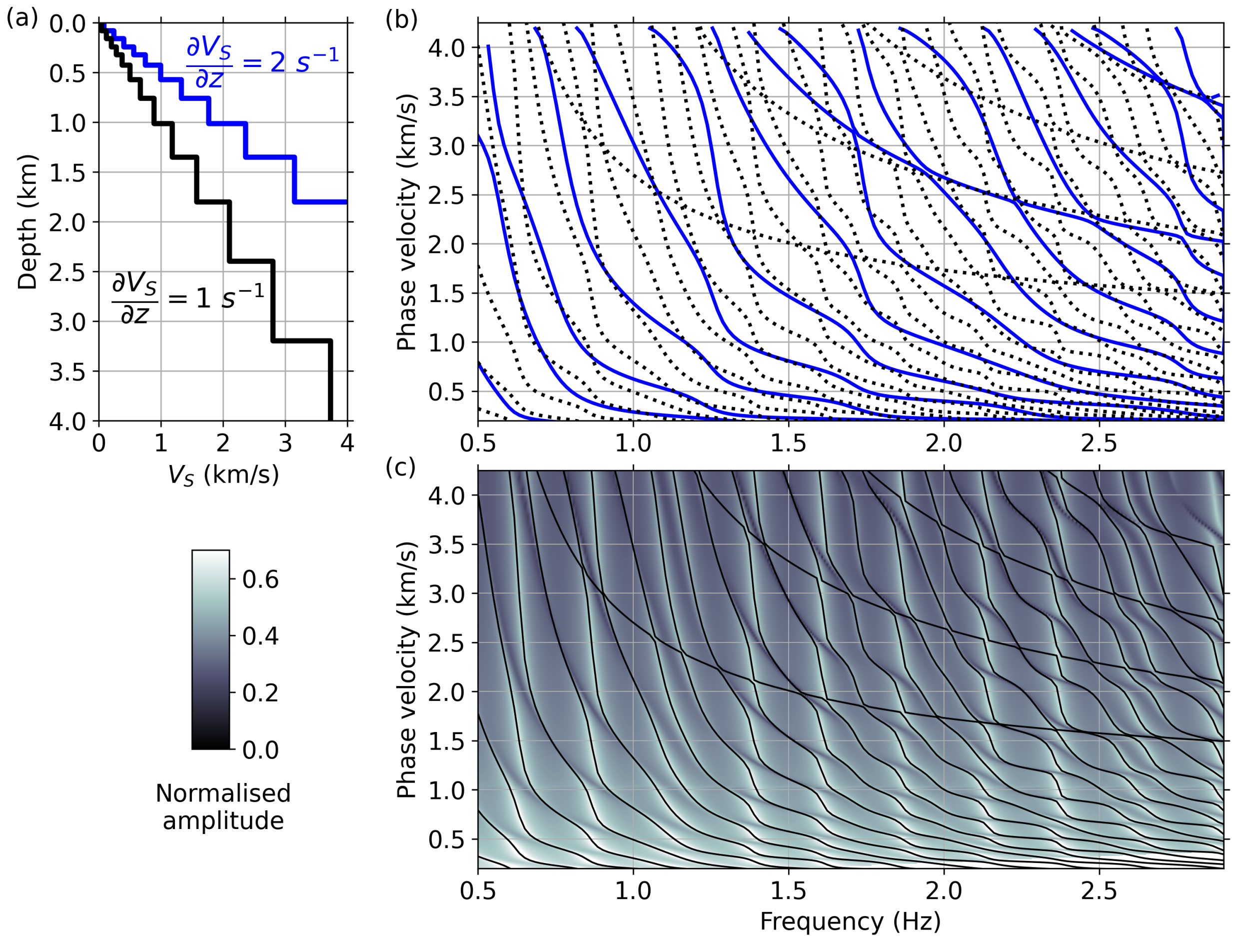

Figure 6. (a) Velocity models for two constant V_S gradients ($^{\Delta V_S}/_{\Delta z} = 1,\ 2\ s^{-1}$). (b) Theoretical DCs for the two velocity models shown in (a) using same colour code. (c) Theoretical dispersion image calculated from horizontal strain waveforms excited by an horizontal force and using the velocity model with a gradient of $^{\Delta V_S}/_{\Delta z}$ =1 s^{-1}. The amplitude of the energy is normalised between 0 and 1 and the DCs from (b) are shown by the black lines.

We consider two velocity models with different V_S gradients with depth (Figure 6a). The two gradients are defined as $^{\Delta V_S}/_{\Delta z}$ =1 s^{-1} and $^{\Delta V_S}/_{\Delta z}$ =2 s^{-1}, where ΔV_S and Δz are the S-wave velocity and depth of each layer. For the two gradient models, the layer thickness (h) is proportional to its depth (z) and is defined as $h \approx z/3$. The density and compressional-wave velocity (V_P) are obtained for each layer from V_S through empirical relationships (Berteussen 1977; Brocher 2005). Surface-wave DCs for the two V_S gradient media are computed following the method introduced in Perton & Sánchez-Sesma (2016) and depict different behaviours (Figure 6b). First, the number of modes is inversely proportional to the V_S gradient value. Second, several parts of the DCs obtained with both gradients are superimposed. Third, apparent DCs, which are constituted of a succession of osculation points from true DCs, appear in Figure 6b. We observe that the lower the gradient, the lower the velocity of the first apparent DC and the higher the number of apparent DCs for a fixed frequency range.

To better understand the partition of energy in dispersion images, we simulate a dispersion image from horizontal strain waveforms excited by an horizontal force (both along the axis of the cable) obtained with a Discrete Wave Number method (Bouchon 2003) and using a velocity gradient of 1 s^{-1} (Figure 6c). This setup is equivalent to the wavefield recorded by DAS experiments with sub-horizontal fibre-optic cables (Nakahara & Haney 2022). We observe that higher-modes with high energy appear between 0.5 and 3 Hz and that apparent DCs do not hold any energy. The large number of modes combined to the complexity of dispersion images obtained from DAS data makes DC selection and identification difficult. Nevertheless, by picking local energy maxima and not attributing the selected dispersion points to DCs, we minimise the risk of mode miss-identification.

We also investigate the energy partition in dispersion images computed from vertical displacement waveforms generated by a vertical source, which is the equivalent of a dispersion image that could be obtained from the vertical component of OBSs (Figure S3). In this case, apparent DCs hold most of the energy and could easily be mistaken for true DCs. Therefore, special care is recommended when selecting DCs from CCFs computed from the vertical component of dense OBS networks, as mistaking apparent DCs for true DCs would undeniably lead to biased estimates of the velocity structure.

3.5 Multi-mode inversion scheme

3.5.1 Resolution of DAS dispersion images

The number of modes that can be retrieved from dispersion images depends on the array aperture (e.g., Section 3.2) and the velocity gradient in the medium (e.g., Section 3.4). Therefore, it is critical to observe a convergence of the number of modes in dispersion images to avoid finding a gradient value that is representative of the array aperture and not of the medium properties.

Here, we observe a stable number of modes for phase velocities above 1 km/s by considering 400 receivers (Figure 4b).

The slant-stack algorithm has a velocity resolution of $\Delta x/\Delta t$, where Δx and Δt are the channel spacing and temporal sampling of the CCFs, respectively (e.g., similar to the frequency-wavenumber ($f-k$) resolution described in Ventosa et al. 2012). In our experiment setting, the slowest velocity difference that can be resolved is 51 m/s as Δx and Δt are equal to 5.1 m and 0.1 s, respectively. In addition, we note that for a gradient velocity medium, the number of DCs significantly increases at slow velocities with increasing frequency (e.g., below 0.25 km/s in Figure 6b). This leads to DCs that cannot be separated at high frequencies due to the limited resolution of the phase velocity discretisation. To account for these limitations, we define a function to automatically reject dispersion points slower than a given phase velocity c_{min} as

$$c_{min} = \begin{cases} 250 \text{ m/s for } f <= 1 \text{ Hz} \\ (250 + 0.025 \times (f-1)) \text{ m/s for } f > 1 \text{ Hz} . \end{cases} \tag{3}$$

The effect of the data selection process is shown in Figure 5, where no dispersion points are selected for velocities below c_{min}.

3.5.2 *Objective function*

The selected dispersion points are considered independently as their identification into separated DCs is difficult, especially at high frequencies. A drawback of this approach is that the inversion of a large number of dispersion points can easily be biased. A popular misfit function used to perform multi-mode inversions is the root mean square (RMS) function (Perton et al. 2019). The RMS function can be defined as

$$\epsilon_{DC}^2 = \frac{1}{J_{max}} \sum_{f=f_{min}}^{f_{max}} \sum_{j=0}^{j_{max}} \sum_{n=0}^{n_{max}} G\left(\left|c_j^{obs}(f) - c_n^{th}(f)\right|\right)^2 , \tag{4}$$

where n is the number of theoretical modes and j the number of observed dispersion points at a frequency f. J_{max} is the number of selected dispersion points in a specific frequency band (i.e., $J_{max} = \sum_{f=f_{min}}^{f_{max}} j_{max}(f)$). c^{th} and c_j^{obs} are the phase velocities of the theoretical and observed DCs, respectively. G is a function that considers if a theoretical dispersion point matches a selected dispersion point and is defined as

$$G(x) = \begin{cases} x & \text{when} \quad |x| \leq \delta \\ \delta & \text{when} \quad |x| > \delta \end{cases}, \tag{5}$$

where δ is a threshold value that is equal to the mean velocity difference between the observed dispersion points. Nonetheless, Equation 4 does not perform well for inverting a large number of selected dispersion points. We systematically converge toward a low velocity gradient medium with a large number of inverted DCs that directly minimise the misfit function (Figure S4).

To overcome this problem, we modify the misfit function to penalise configurations that use more theoretical modes than the number of selected points at each frequency and in specific phase velocity ranges (e.g., c_{min} to c_{max}). The phase velocity range is defined as the area where we confirmed the retrieval of all modes given the 2040 m array aperture. Note that c_{max} is fixed to 2 km/s as the slope of DCs above this value is too strong for dispersion points to be accurately resolved. We define n_{min} as the number of the first theoretical mode with a velocity above c_{min} and n_{max} as the number of the last theoretical mode with a phase velocity below c_{max}. As the number of theoretical modes between n_{min} and n_{max} is $n_{max} - n_{min}$ and the number of observed points is j_{max}, we weight the misfit function with $|n_{max} - n_{min} - j_{max}|$. The final misfit function is therefore defined as

$$\epsilon^2_{DC} = \frac{1}{j_{max}} \sum_{f=f_{min}}^{f_{max}} \sum_{n=0}^{j_{max}} \sum_{n=0}^{n_{max}} G\left(\left|c_j^{obs}(f) - c_n^{th}(f)\right|\right)^2 \left(1 + \frac{|n_{max} - n_{min} - j_{max}|}{j_{max}}\right). \tag{6}$$

This functional form adapts to the changing modal content and operates well at all position along the cable.

3.5.3 *Parametrisation*

We start the inversion for the selected dispersion points at virtual source 3000. We use a constant gradient of ${}^{\Delta V_S}/_{\Delta z} = 0.8\ s^{-1}$ as the starting velocity profile and consider the gradient value as the only free parameter. After obtaining the gradient value, we first invert for the thickness of each layer and then, separately, for their shear-wave velocity. Since surface waves have a low sensitivity to density and V_P, we estimate them from V_S through empirical relationships (Berteussen 1977;

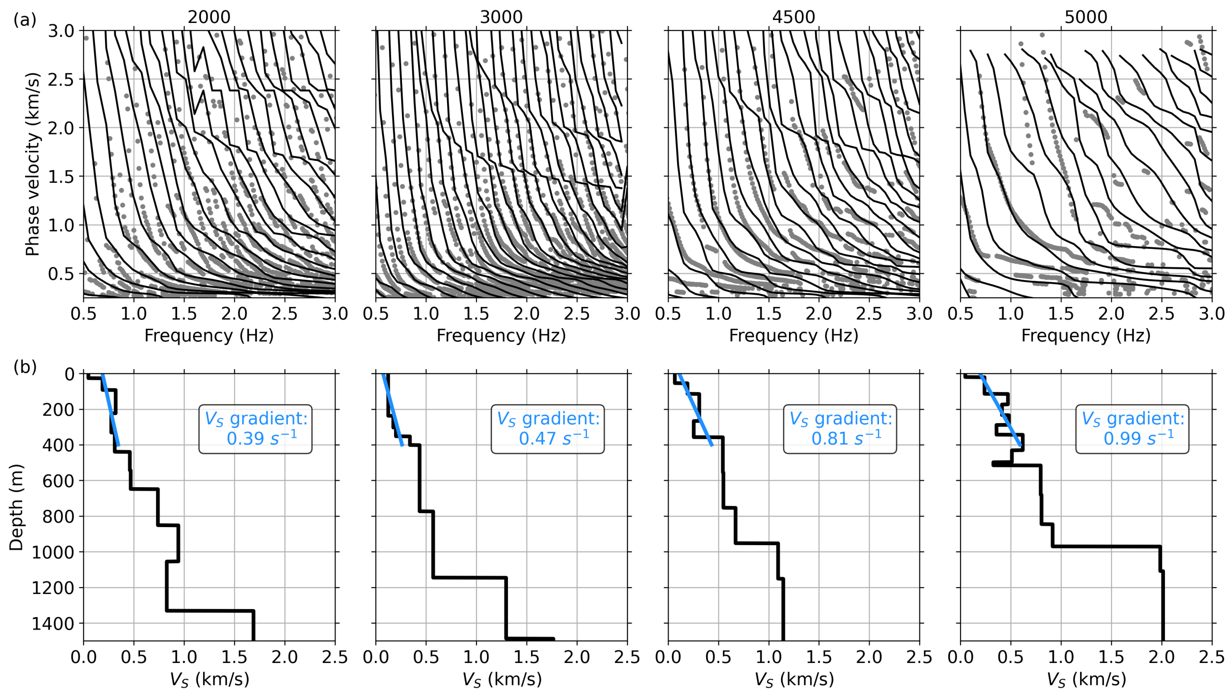

Figure 7. (a) Selected dispersion points (grey dots) and inverted DCs (black lines) for four sections along the cable. The virtual source number is indicated on top of each subplot. (b) Inverted V_S velocity model (black) for the four sections shown in (a). V_S gradient values and lines computed between the ocean floor and 400 m depth are shown in blue.

Brocher 2005). Similarly to Perton et al. (2019), we use a constrained nonlinear optimisation procedure to minimise the misfit function (Byrd et al. 1999). We impose the highest velocity to be in the half-space as it helps to compute more stable DCs. We then use the inverted velocity profile at channel 3000 as the input model for the neighbouring virtual sources and iteratively invert the selected dispersion points along the cable from virtual sources 1500 to 8000.

4 RESULTS AND DISCUSSION

4.1 On the reliability of the inversion

We show the 1-D inversion results at four virtual sources along the cable in Figure 7. The inverted DCs fit well most of the selected points (Figure 7a), which provides confidence in the inverted 1-D velocity models shown in Figure 7b. Apparent DCs appear in the fitted DCs for the four virtual sources, but are not visible in the selected dispersion points. This difference can be explained by the simulations performed in Section 3.4, where we show that apparent DCs do not hold much energy for DAS-like deformation dispersion images (Figure 6c). Therefore, we do not expect the selected dispersion points to contain the signature of apparent DCs.

The misfit function minimised by Equation 6 does not allow us to estimate the reliability of the inversion along the array as the weights change with the number of fitted DCs. To provide misfit estimates that can be compared along the array, we compute misfit values from the final inversion results using Equation 4 and show them in Figure 8a. We observe relatively constant misfit values along the cable with a mean value of 90 and a one standard deviation to the mean of 23. The results from a few individual virtual sources have larger misfit values, but their inverted velocity models are consistent with the neighbouring ones, which demonstrates the stability of the velocity model along the array.

4.2 2-D shear-wave velocity model, bathymetry, and their effect on the modal content

The final inverted 2-D velocity model is shown in Figure 9a. The model is smoothed using the median value of a 2-D sliding window (i.e., horizontal and vertical). The lengths of the smoothing window are 408 and 20 m in the horizontal and vertical directions, respectively. Along the array, V_S is generally relatively slow near the ocean bottom (e.g., $<$200 m/s) and increases with depth. A stiffer material with a velocity of 2500 m/s is observed at a depth of 1000-1500 m below the ocean floor.

The modal content of dispersion images significantly varies along the array. In Figure 8b, we show the number of fitted DCs at 2 Hz, which is a proxy for evaluating the modal content of dispersion images over the whole spectrum. We observe the largest number of fitted DCs between channels 2000 and 3000, with over 25 modes at some stations. The number of modes then decreases to approximately 10 modes near channel 5500. To better understand the impact of shallow layers on the modal content, we compute a V_S gradient value between the ocean floor and 400 m depth for each 1-D model. V_S gradients are defined as the slope of a straight line fitted to each V_S 1-D profile between the surface and 400 m depth. Examples of V_S gradient lines and values are shown in Figure 7b. In Figure 8c, we show V_S gradient values along the array after applying

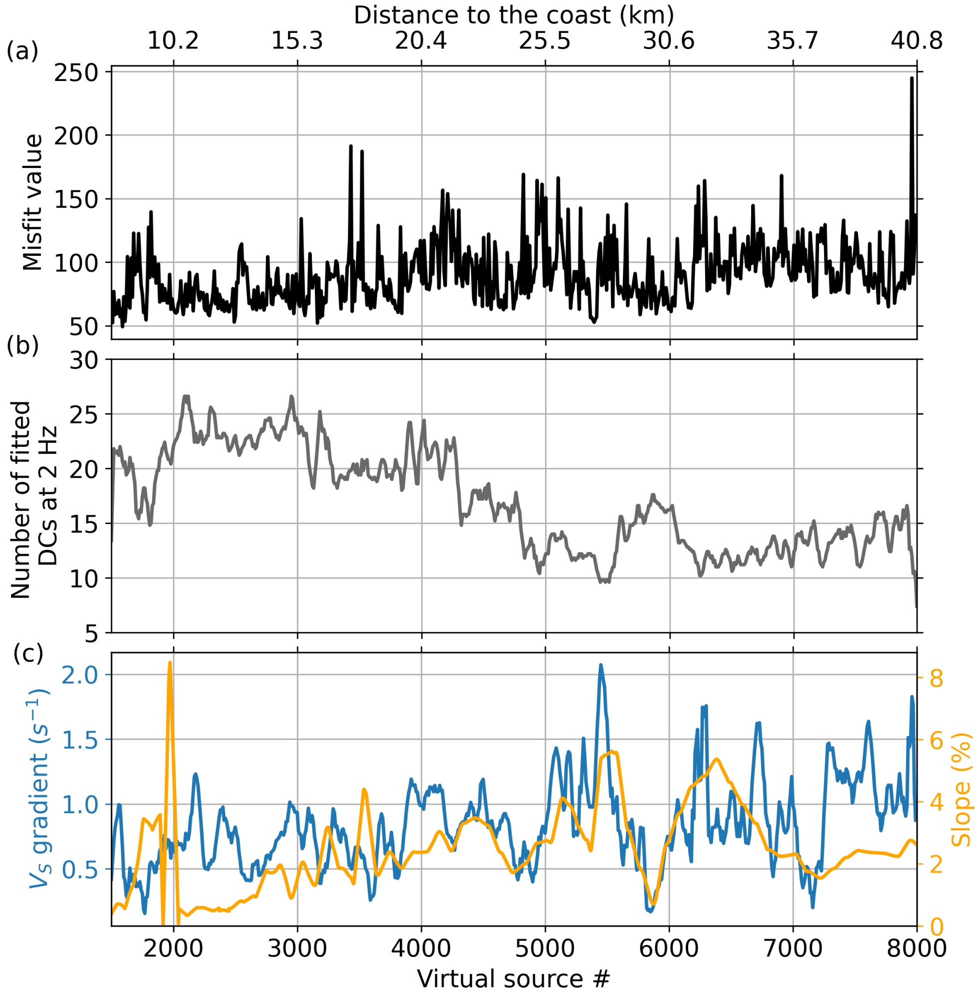

Figure 8. (a) Misfit value along the cable computed using Equation 4 from the final inverted DCs. (b) Number of fitted modes for each dispersion image at a frequency of 2 Hz. (c) V_S gradient value calculated between the ocean floor and 400 m depth (blue) and the slope of the bathymetry (orange).

a lateral smoothing over ten 1-D models. V_S gradients oscillate between 0.3 and 1.2 s^{-1} between channels 1500 to 4500, peak to 2.1 s^{-1} near channel 5500, and finally oscillate between 0.3 and 1.75 s^{-1} until channel 8000. We observe an anti-correlation between the number of fitted DCs and V_S gradients. This shows that rapidly increasing velocities in the medium lead to dispersion images with less surface-wave modes. This observation agrees with the theoretical results obtained in Section 3.4 for gradient media.

Changes of bathymetry can have a direct impact on the velocity structure, and therefore, on the modal content of dispersion images. To characterise this effect, we show the slope of the bathymetry in Figure 8c. The slope is defined as the ratio between the vertical distance over an horizontal distance between two points, multiplied by 100. In this study, the slope is computed along the array using a sliding horizontal distance of 408 m. We observe a good correlation between the slope of the bathymetry and V_S gradient values. Flat sections of the cable, where the slope is less than 4%, generally coincide with slow V_S gradient values and more fitted DCs. Moreover, the region between channels 5000 and 5500, where spatial aliasing appears in the dispersion images, coincides with the region where the largest gradient values are observed. This demonstrates that the number of selected dispersion points and the presence/absence of spatial aliasing are closely related to the nature of the sediments in the shallow subsurface.

4.3 Comparison with another velocity model

We compare the inverted velocity model with that obtained by Spica et al. (2020), which was obtained from data of the same fibre-optic cable, in Figure 9. We observe a good agreement between the two models between channels 5000 and 8400, with a similar shallow structure and a bedrock located approximately at the same depth (i.e., between 1 and 2 km below the ocean floor). Between channels 2500 and 4500, both models agree well at shallow depth with a very slow V_S layer. The main discrepancy between the two models resides in the depth of the bedrock between channels 1500 and 5000. While the model from this study shows a bedrock depth constantly deeper than 1 km below the ocean floor, the Spica et al. (2020) model displays a very shallow bedrock in this region. The discrepancies between the two models can be explained by the different processing steps and inversion schemes applied to the DAS data. The Spica et al. (2020) model was computed by inverting phase velocity DCs obtained from $f-k$ power spectra sliding over the array. Each $f-k$ spectrum was computed over 600 channels (i.e, 3060 m), every 200 m, and DCs were extracted between 0.2 and 1 Hz. Moreover, the inversion of the Spica et al. (2020) model was performed for the thickness and V_S of two layers overlying a half-space, and by only using the fundamental and first higher-modes of surface waves. This distinct data processing naturally provides a lower resolution of their model compared to the multi-mode inversion scheme used in this study.

It is well established that surface-wave DCs are sensitive to the absolute velocity in the medium and generally provide a non-unique solution of the layered structure (Scherbaum et al. 2003). This

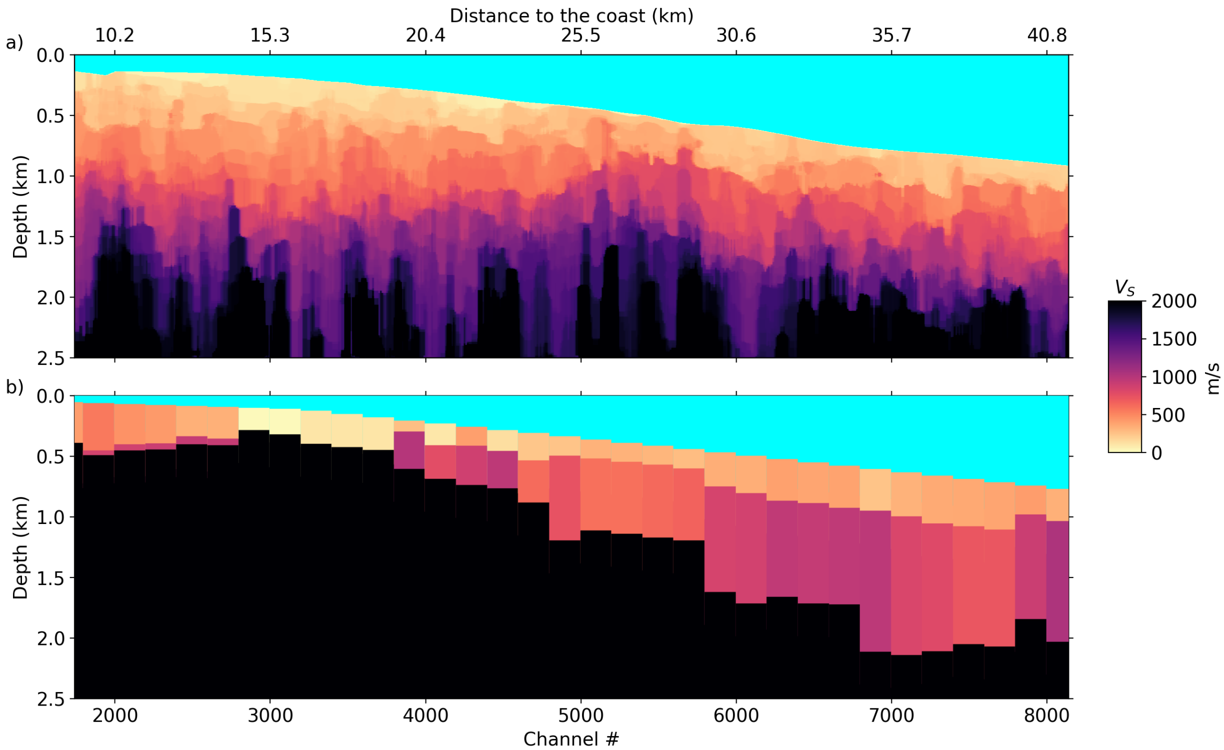

Figure 9. (a) Inverted velocity model and (b) the velocity model obtained by Spica et al. (2020). The V_S velocity is clipped at 2500 m/s for both models.

is mainly caused by the broad sensitivity kernels of surface waves which sample a wide range of depths depending on their frequency. Nevertheless, surface-wave inversions can be better constrained by adding different observables (Lin et al. 2012; Spica et al. 2017, 2018), or a larger number of higher modes sensitive to different depths. In the Spica et al. (2020) study, only the fundamental mode of Scholte waves was retrieved between channels 1500 and 5000 and the fundamental and first-higher modes after channel 5000. Therefore, the velocity model presented in this study is likely more accurate and better constrained before channel 5000 as we retrieve and use a large number of surface-wave modes with clear dispersive features up to phase velocities of 3 km/s. Moreover, the similarity between the two velocity models after channel 5000 can be explained by the fact that both velocity structures are obtained by inverting multiple surface-wave modes, which provides a better sensitivity at greater depths.

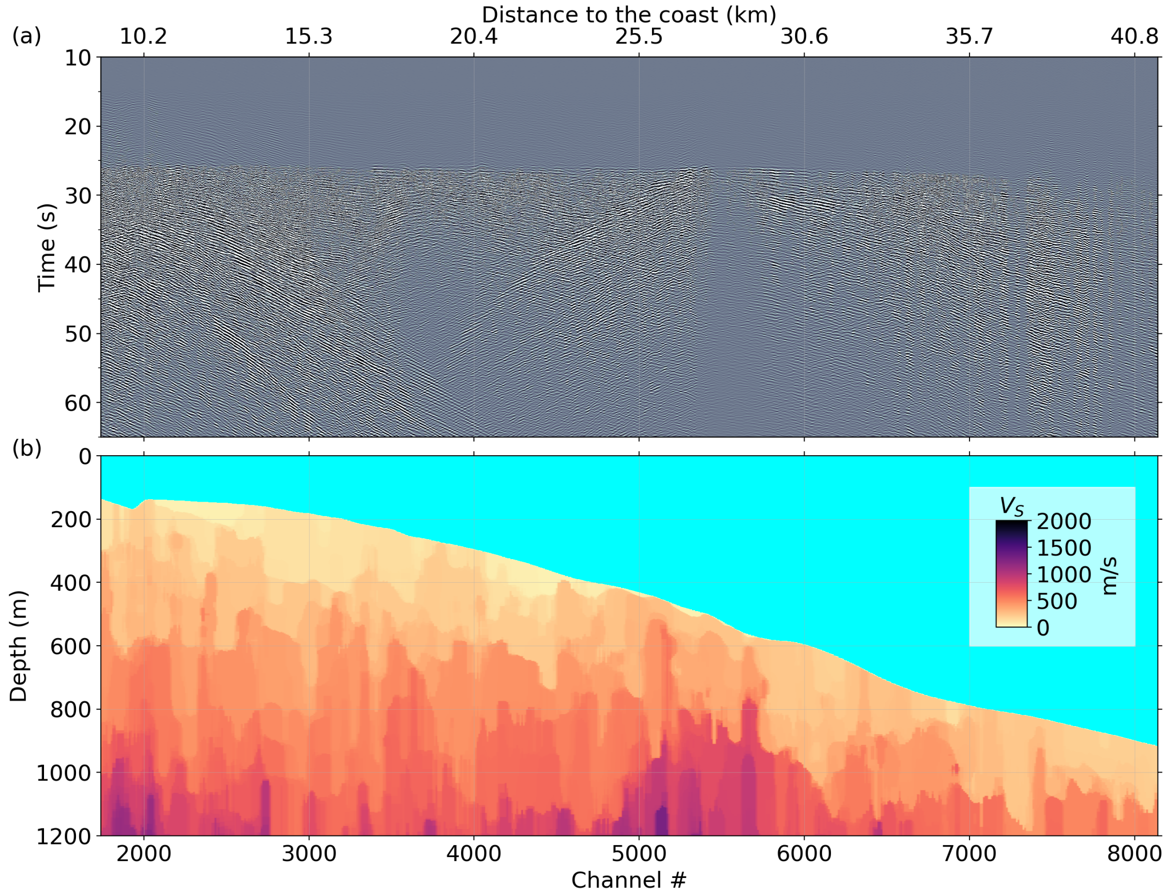

Figure 10. (a) Strain waveforms of a M_w 3.7 earthquake bandpass filtered between 1 and 3 Hz (location in Figure 1). P- and S-waves arrive around 15 s and 25 s after the origin time, respectively. (b) Zoom on the shallow part of the inverted velocity model.

4.4 Effects on the earthquake wavefield

Numerous local and regional earthquakes were recorded during the two-week time period of the DAS experiment. In Figure 10, we show the strain waveforms of a moment magnitude (M_w) 3.7 earthquake bandpass filtered between 1 and 3 Hz. The earthquake occurred on November 21, 2019 at 16:29:13 (UTC) at a depth of 33 km (National Research Institute for Earth Science and Disaster Prevention centroid moment tensor solution) and its location is shown in Figure 1. The direct P-wave arrives around 15 s but is barely visible as it propagates nearly orthogonally to the cable (Martin et al. 2021). On the other hand, the direct S-wave arrives between 25 and 30 s and can be observed at all channels. In addition, we also observe strong surface waves generated after the direct S-wave arrival near channels 2000 and 5300.

On the ocean bottom, surface waves can be excited locally by a variety of phenomena, including body-wave scattering caused by sharp changes of the bathymetry (Zheng et al. 2013), strong lateral heterogeneities such as fault zones (Sato et al. 2012), and water phase reverberations (Spica et al. 2022). Figures 10 and S5 show that surface waves are generally excited at the same two locations during earthquakes. These two locations are characterised by very soft and shallow V_S layers and relatively sharp bathymetry changes. Therefore, a combined effect of soft and shallow layers and bathymetry changes is likely responsible for the generation of surface waves in these two regions. We also note that the amplitude of seismic waves is very small near channel 5500. This can be explained by the relatively high V_S layers in the shallow subsurface below these stations, which do not have the potential to trap and amplify incoming high-frequency seismic waves. In contrast, the ground motions near channel 3000, where the structure is characterised by very slow V_S layers over the first 200 m, exhibit large amplifications that last beyond 50 s after the P-wave arrival. This strong and lasting wave amplification can be explained by seismic waves trapped in the shallow structure.

5 CONCLUSIONS

We retrieved surface waves by cross-correlating continuous strain signals recorded along a fibre-optic cable offshore the Sanriku Coast, Japan. We first analysed the effect of data pre-processing on the retrieval of dispersion images and concluded that computing 1-bit CCFs and considering 400 receiver channels (i.e., 2040 m array aperture) offer a good trade-off between mode separation and lateral spatial resolution. We then presented a theoretical case to shade some lights on the complexity of dispersion images computed from DAS data using constant V_S gradient media. Our simulations confirmed that gradient media, which are representative of marine sediments, can generate a large number of surface wave modes. Based on data processing and theoretical considerations, we inverted surface-wave DCs to provide a 2-D model of the V_S structure. We found that shallow low-velocity layers combine with bathymetry changes can greatly impact the modal content of surface waves. We finally compared the inverted V_S model with that from Spica et al. (2020) and discussed the effect of the shallow structure on the propagation of earthquake seismic waves.

OBDAS provides a unique opportunity to image marine sediments with an unprecedented spatial resolution and to better understand the seismic wavefield. Moreover, OBDAS has the potential to greatly improve earthquake early warning systems in subduction zones by rapidly detecting events and estimating their magnitudes. While there is no doubt that earthquakes can be detected by OBDAS arrays, rapid magnitude estimation is likely to be more challenging due to the complexity of the recorded wavefield. Nevertheless, imaging the shallow subsurface beneath fibre-optic cables will lower such uncertainties by providing better constrains on local seismic wave amplifications. Finally, the methodology presented in this study is readily applicable to onshore metropolitan areas characterised by shallow and low V_S sediments that can significantly amplify earthquake ground motions, such as Mexico city, Jakarta, Taipei, and Los Angeles.

ACKNOWLEDGMENTS

We thank Takeshi Akuhara for providing useful information about the targeted area and DAS measurements. We thank *Fujitsu* for cooperating with the Earthquake Research Institute (ERI), The University of Tokyo, for the DAS measurement campaigns. All the Figures are plotted with Matplotlib (Hunter 2007) or the Generic Mapping Tool (Wessel et al. 2019). Some of the data processing steps have been performed using ObsPy (Beyreuther et al. 2010). **Funding:** This project was partly supported by the discretionary budget of the director of ERI. The observations were carried out as part of the Earthquake and Volcano Hazards Observation and Research Program by the Ministry of Education, Culture, Sports, Science, and Technology of Japan. L.V is supported by NSF award EAR2022716 and M.P is supported by CONACyT award CF-2019-G-6655. Z.J.S acknowledges support from the Air Force Research Laboratory grant FA9453-21-2-0018. **Competing interests:** The authors declare that they have no competing interests.

DATA AVAILABILITY

The CCFs, 2-D velocity model, and codes developed to perform the technical analysis and to reproduce most figures of the paper will be made publicly available after review and before eventual acceptance of the manuscript.

REFERENCES

Aki, K. & Richards, P., 2002. *Quantitative Seismology*, Geology (University Science Books).: Seismology, University Science Books.

Ali, B. H. & Broadhead, M. K., 1995. *Full Field Inversion Methods in Ocean- and Seismo-Acoustics*, Kluwer Academic, Dordrecht.

Aoi, S., Asano, Y., Kunugi, T., Kimura, T., Uehira, K., Takahashi, N., Ueda, H., Shiomi, K., Matsumoto, T., & Fujiwara, H., 2020. Mowlas: Nied observation network for earthquake, tsunami and volcano, *Earth, Planets and Space*, **72**(1), 126.

Bensen, G. D., Ritzwoller, M. H., Barmin, M. P., Levshin, A. L., Lin, F., Moschetti, M. P., Shapiro, N. M., & Yang, Y., 2007. Processing seismic ambient noise data to obtain reliable broad-band surface wave dispersion measurements, *Geophys. J. Int.*, **169**, 1239–1260.

Berteussen, K.-A., 1977. Moho depth determinations based on spectral-ratio analysis of norsar long-period p waves, *Physics of the Earth and Planetary Interiors*, **15**(1), 13–27.

Beyreuther, M., Barsch, R., Krischer, L., Megies, T., Behr, Y., & Wassermann, J., 2010. ObsPy: A Python Toolbox for Seismology, *Seism. Res. Lett.*, **81**(3), 530–533.

Bouchon, M., 2003. A review of the discrete wavenumber method, *Pure Appl. Geophys.*, **160**(3), 445–465.

Brocher, T. M., 2005. Empirical Relations between Elastic Wavespeeds and Density in the Earth's Crust, *Bull. Seismol. Soc. Am.*, **95**(6), 2081–2092.

Bussat, S. & Kugler, S., 2011. Offshore ambient-noise surface-wave tomography above 0.1 hz and its applications, *The Leading Edge*, **30**(5), 514–524.

Byrd, R., Hribar, M., & Nocedal, J., 1999. An interior point algorithm for large-scale nonlinear programming, *SIAM Journal on Optimization*, **9**(4), 877–900.

Castellanos, J. C., Clayton, R. W., & Pérez-Campos, X., 2018. Imaging the eastern trans-mexican volcanic belt with ambient seismic noise: Evidence for a slab tear, *J. Geophys. Res. Solid Earth*, **123**, 7741–7759.

Cedilnik, G., Lees, G., Schmidt, P., Herstrøm, S., & Geisler, T., 2019. Ultra-long reach fiber distributed acoustic sensing for power cable monitoring, *10th International Conference on Insulated Power Cables*.

Cheng, F., Chi, B., Lindsey, N. J., Dawe, T. C., & Ajo-Franklin, J. B., 2021. Utilizing distributed acoustic sensing and ocean bottom fiber optic cables for submarine structural characterization, *Scientific reports*, **11**(1), 1–14.

Dai, T., Hu, Y., Ning, L., Cheng, F., & Pang, J., 2018. Effects due to aliasing on surface-wave extraction and suppression in frequency-velocity domain, *Journal of Applied Geophysics*, **158**, 71–81.

de Ridder, S. & Dellinger, J., 2011. Ambient seismic noise eikonal tomography for near-surface imaging at valhall, *The Leading Edge*, **30**(5), 506–512.

Foti, S., Lai, C., Rix, G., & Strobbia, C., 2015. *Surface wave methods for near-surface site characterization*, CRC Press, Boca Raton, Fla.

Glorieux, C., Van de Rostyne, K., Nelson, K., Gao, W., Lauriks, W., & Thoen, J., 2001. On the character of acoustic waves at the interface between hard and soft solids and liquids, *The Journal of the Acoustical Society of America*, **110**(3), 1299–1306.

Gusev, V., Desmet, C., Lauriks, W., Glorieux, C., & Thoen, J., 1996. Theory of scholte, leaky rayleigh, and lateral wave excitation via the laser-induced thermoelastic effect, *The Journal of the Acoustical Society of America*, **100**(3), 1514–1528.

Hamilton, E. L., 1979. Sound velocity gradients in marine sediments, *The Journal of the Acoustical Society of America*, **65**(4), 909–922.

Hartog, A., 2017. *An Introduction to Distributed Optical Fibre Sensors*, CRC Press.

Hayes, G. P., Moore, G. L., Portner, D. E., Hearne, M., Flamme, H., Furtney, M., & Smoczyk, G. M., 2018. Slab2, a comprehensive subduction zone geometry model, *Science*, **362**(6410), 58–61.

Hunter, J. D., 2007. Matplotlib: A 2d graphics environment, *Computing In Science & Engineering*, **9**(3), 90–95.

Ide, S., Araki, E., & Matsumoto, H., 2021. Very broadband strain-rate measurements along a submarine fiber-optic cable off cape muroto, nankai subduction zone, japan, *Earth, Planets and Space*, **73**(1), 1–10.

Kanazawa, T. & Hasegawa, A., 1997. Ocean-bottom observatory for earthquakes and tsunami off sanriku, north-east japan using submarine cable, *International Workshop on Scientific Use of Submarine Cables, Comm. for Sci. Use of Submarine Cables, Okinawa, Japan, 1997*, pp. 208–209.

Karrenbach, M., Ellwood, R., Yartsev, V., Araki, E., Kimura, T., & Matsumoto, H., 2020. Long-range das data acquisition on a submarine fiber-optic cable, *EAGE Workshop on Fiber Optic Sensing for Energy Applications in Asia Pacific*, **2020**(1), 1–5.

Lin, F.-C., Ritzwoller, M. H., Townend, J., Bannister, S., & Savage, M. K., 2007. Ambient noise Rayleigh wave tomography of New Zealand, *Geophys. J. Int.*, **170**(2), 649–666.

Lin, F.-C., Schmandt, B., & Tsai, V. C., 2012. Joint inversion of rayleigh wave phase velocity and ellipticity using usarray: Constraining velocity and density structure in the upper crust, *Geophys. Res. Lett.*, **39**(12).

Lindsey, N. J., Dawe, T. C., & Ajo-Franklin, J. B., 2019. Illuminating seafloor faults and ocean dynamics with dark fiber distributed acoustic sensing, *Science*, **366**(6469), 1103–1107.

Lior, I., Sladen, A., Rivet, D., Ampuero, J.-P., Hello, Y., Becerril, C., Martins, H. F., Lamare, P., Jestin, C., Tsagkli, S., & Christos, M., 2021. On the Detection Capabilities of Underwater Distributed Acoustic Sensing, *Journal of Geophysical Research: Solid Earth*, **126**(3), e2020JB020925.

Lior, I., Mercerat, E. D., Rivet, D., Sladen, A., & Ampuero, J., 2022. Imaging an Underwater Basin and Its Resonance Modes Using Optical Fiber Distributed Acoustic Sensing, *Seism. Res. Lett.*.

Martin, E. R., Lindsey, N. J., Ajo-Franklin, J. B., & Biondi, B. L., 2021. *Introduction to Interferometry of Fiber-Optic Strain Measurements*, chap. 9, pp. 111–129, American Geophysical Union (AGU).

Matsumoto, H., Araki, E., Kimura, T., Fujie, G., Shiraishi, K., Tonegawa, T., Obana, K., Arai, R., Kaiho, Y., Nakamura, Y., et al., 2021. Detection of hydroacoustic signals on a fiber-optic submarine cable, *Scientific reports*, **11**(1), 1–12.

Mordret, A., Landès, M., Shapiro, N., Singh, S., Roux, P., & Barkved, O., 2013. Near-surface study at the valhall oil field from ambient noise surface wave tomography, *Geophysical Journal International*, **193**(3), 1627–1643.

Mordret, A., Landès, M., Shapiro, N. M., Singh, S. C., & Roux, P., 2014. Ambient noise surface wave tomography to determine the shallow shear velocity structure at Valhall: depth inversion with a Neighbourhood Algorithm, *Geophys. J. Int.*, **198**, 1514–1525.

Nakahara, H. & Haney, M. M., 2022. Connection between the cross correlation and the Green's function: strain and rotation of surface waves, *Geophys. J. Int.*, ggac094.

Nayak, A., Ajo-Franklin, J., & Team, T. I. V. D. F., 2021. Measurement of Surface-Wave Phase-Velocity Dispersion on Mixed Inertial Seismometer – Distributed Acoustic Sensing Seismic Noise Cross-Correlations, *Bull. Seismol. Soc. Am.*, **111**(6), 3432–3450.

Nishida, K., Kawakatsu, H., & Obara, K., 2008. Three-dimensional crustal S wave velocity structure in Japan using microseismic data recorded by Hi-net tiltmeters, *J. Geophys. Res. Solid Earth*, **113**, B10302.

Park, C. B., Miller, R. D., & Xia, J., 1998. *Imaging dispersion curves of surface waves on multi-channel record*, pp. 1377–1380.

Perton, M. & Sánchez-Sesma, F. J., 2016. Green's function calculation from equipartition theorem, *The Journal of the Acoustical Society of America*, **140**(2), 1309–1318.

Perton, M., Spica, Z. J., Clayton, R. W., & Beroza, G. C., 2019. Shear wave structure of a transect of the Los Angeles basin from multimode surface waves and H/V spectral ratio analysis, *Geophys. J. Int.*, **220**(1), 415–427.

Rivet, D., de Cacqueray, B., Sladen, A., Roques, A., & Calbris, G., 2021. Preliminary assessment of ship detection and trajectory evaluation using distributed acoustic sensing on an optical fiber telecom cable, *The Journal of the Acoustical Society of America*, **149**(4), 2615–2627.

Sabra, K. G., Gerstoft, P., Roux, P., Kuperman, W. A., & Fehler, M. C., 2005. Extracting time-domain Green's function estimates from ambient seismic noise, *Geophys. Res. Lett.*, **32**, L03310.

Sato, H., Fehler, M. C., & Maeda, T., 2012. *Seismic wave propagation and scattering in the heterogeneous Earth*, vol. 496, Springer.

Scherbaum, F., Hinzen, K.-G., & Ohrnberger, M., 2003. Determination of shallow shear wave velocity profiles in the Cologne, Germany area using ambient vibrations, *Geophys. J. Int.*, **152**(3), 597–612.

Schimmel, M. & Paulssen, H., 1997. Noise reduction and detection of weak, coherent signals through phase-weighted stacks, *Geophys. J. Int.*, **130**, 497–505.

Shapiro, N. M. & Campillo, M., 2004. Emergence of broadband Rayleigh waves from correlations of the ambient seismic noise, *Geophys. Res. Lett.*, **31**, L07614.

Shinohara, M., Yamada, T., Akuhara, T., Mochizuki, K., Sakai, S., Hamakawa, M., Kasajima, T., Arioka, T., & Kubota, S., 2019. Distributed acoustic sensing measurement by using seafloor optical fiber cable system off sanriku for seismic observation, in *OCEANS 2019 MTS/IEEE SEATTLE*, pp. 1–4.

Shinohara, M., Yamada, T., Uehira, K., Sakai, S., Shiobara, H., & Kanazawa, T., 2021. Development and operation of an ocean bottom cable seismic and tsunami (obcst) observation system in the source region of the tohoku-oki earthquake, *Earth and Space Science*, **8**(3), e2020EA001359, e2020EA001359 2020EA001359.

Shinohara, M., Yamada, T., Akuhara, T., Mochizuki, K., & Sakai, S., 2022. Performance of seismic observation by distributed acoustic sensing technology using a seafloor cable off sanriku, japan, *Front. Mar. Sci.*.

Sladen, A., Rivet, D., Ampuero, J.-P., De Barros, L., Hello, Y., Calbris, G., & Lamare, P., 2019. Distributed sensing of earthquakes and ocean-solid earth interactions on seafloor telecom cables, *Nature Communications*, **10**(1), 1–8.

Socco, L. & Strobbia, C., 2004. Surface-wave method for near-surface characterization: a tutorial, *Near Surface Geophysics*, **2**(4), 165–185.

Spica, Z., Perton, M., Calò, M., Legrand, D., Córdoba-Montiel, F., & Iglesias, A., 2016. 3-D shear wave velocity model of Mexico and South US: bridging seismic networks with ambient noise cross-correlations (C1) and correlation of coda of correlations (C3), *Geophys. J. Int.*, **206**(3), 1795–1813.

Spica, Z., Perton, M., Nakata, N., Liu, X., & Beroza, G. C., 2018. Shallow VS Imaging of the Groningen Area from Joint Inversion of Multimode Surface Waves and H/V Spectral Ratios, *Seism. Res. Lett.*, **89**(5), 1720–1729.

Spica, Z. J., Perton, M., Nakata, N., Liu, X., & Beroza, G. C., 2017. Site characterization at Groningen gas field area through joint surface-borehole H/V analysis, *Geophys. J. Int.*, **212**(1), 412–421.

Spica, Z. J., Nishida, K., Akuhara, T., Pétrélis, F., Shinohara, M., & Yamada, T., 2020. Marine sediment characterized by ocean-bottom fiber-optic seismology, *Geophys. Res. Lett.*, **47**(16), e2020GL088360, e2020GL088360 10.1029/2020GL088360.

Spica, Z. J., Castellanos, J. C., Viens, L., Nishida, K., Akuhara, T., Shinohara, M., & Yamada, T., 2022. Subsurface imaging with ocean-bottom distributed acoustic sensing and water phases reverberations, *Geophys. Res. Lett.*, **49**(2), e2021GL095287.

Stehly, L., Fry, B., Campillo, M., Shapiro, N. M., Guilbert, J., Boschi, L., & Giardini, D., 2009. Tomography of the Alpine region from observations of seismic ambient noise, *Geophys. J. Int.*, **178**(1), 338–350.

Stein, S. & Wysession, M., 2003. *Introduction to Seismology, Earthquakes, and Earth Structure*, Blackwell Publishing.

Takano, H., Shinohara, M., Nakata, R., Kurashimo, E., Ishiyama, T., & Mochizuki, K., 2021. Seismic reflection survey using seafloor optical cable and das measurement off sanriku, in *Seismological Society* *of Japan Fall Meeting*.

Tonegawa, T., Araki, E., Matsumoto, H., Kimura, T., Obana, K., Fujie, G., Arai, R., Shiraishi, K., Nakano, M., Nakamura, Y., Yokobiki, T., & Kodaira, S., 2022. Extraction of p wave from ambient seafloor noise observed by distributed acoustic sensing, *Geophys. Res. Lett.*, **n/a**(n/a), e2022GL098162, e2022GL098162 2022GL098162.

Ugalde, A., Becerril, C., Villaseñor, A., Ranero, C. R., Fernández-Ruiz, M. R., Martin-Lopez, S., González-Herráez, M., & Martins, H. F., 2021. Noise Levels and Signals Observed on Submarine Fibers in the Canary Islands Using DAS, *Seism. Res. Lett.*, **93**(1), 351–363.

Ventosa, S., Simon, C., & Schimmel, M., 2012. Window length selection for optimum slowness resolution of the local-slant-stack transform, *Geophysics*, **77**(2), V31–V40.

Wang, H. F., Zeng, X., Miller, D. E., Fratta, D., Feigl, K. L., Thurber, C. H., & Mellors, R. J., 2018. Ground motion response to an ML 4.3 earthquake using co-located distributed acoustic sensing and seismometer arrays, *Geophys. J. Int.*, **213**(3), 2020–2036.

Wessel, P., Luis, J. F., Uieda, L., Scharroo, R., Wobbe, F., Smith, W. H. F., & Tian, D., 2019. The generic mapping tools version 6, *Geochemistry, Geophysics, Geosystems*, **20**(11), 5556–5564.

Williams, E. F., Fernández-Ruiz, M. R., Magalhaes, R., Vanthillo, R., Zhan, Z., González-Herráez, M., & Martins, H. F., 2019. Distributed sensing of microseisms and teleseisms with submarine dark fibers, *Nature communications*, **10**(1), 1–11.

Williams, E. F., Fernández-Ruiz, M. R., Magalhaes, R., Vanthillo, R., Zhan, Z., González-Herráez, M., & Martins, H. F., 2021. Scholte wave inversion and passive source imaging with ocean-bottom DAS, *The Leading Edge*, **40**(8), 576–583.

Yao, H., van Der Hilst, R. D., & de Hoop, M. V., 2006. Surface-wave array tomography in SE Tibet from ambient seismic noise and two-station analysis — I. Phase velocity maps, *Geophys. J. Int.*, **166**(2), 732–744.

Zeng, X., Lancelle, C., Thurber, C., Fratta, D., Wang, H., Lord, N., Chalari, A., & Clarke, A., 2017. Properties of Noise Cross-Correlation Functions Obtained from a Distributed Acoustic Sensing Array at Garner Valley, California, *Bull. Seismol. Soc. Am.*, **107**(2), 603–610.

Zheng, Y., Fang, X., Liu, J., & Fehler, M. C., 2013. Scholte waves generated by seafloor topography.

Zhu, J., Popovics, J. S., & Schubert, F., 2004. Leaky rayleigh and scholte waves at the fluid–solid interface subjected to transient point loading, *The Journal of the Acoustical Society of America*, **116**(4), 2101–2110.

Submitted

Supporting Information for
'Understanding surface-wave modal content for high-resolution imaging of submarine sediments with Distributed Acoustic Sensing'

Loïc Viens[1], Mathieu Perton[2], Zack J. Spica[1], Kiwamu Nishida[3], Masanao Shinohara[3], and Tomoaki Yamada[3]

[1] *Department of Earth and Environmental Sciences, University of Michigan, Ann Arbor, Michigan, USA*

[2] *Instituto de Ingeniería, Universidad Nacional Autónoma de México, CDMX, Mexico*

[3] *Earthquake Research Institute, The University of Tokyo, Tokyo, Japan*

15 April 2022

Contents of this file:

(i) Text S1-S5

(ii) Figures S1-S5

Introduction

The supporting information includes:

(i) Text and Figure S1 showing the effect of the number of stations on the spatial aliasing

(ii) Text and Figure S2 displaying the dispersion point selection process

(iii) Text and Figure S3 showing a theoretical dispersion image for vertical waveforms

(iv) Text and Figure S4 discussing the effect of Equations 4 and 5 of the main manuscript on the inverted Dispersion Curves (DCs)

(v) Text and Figure S5 showing the earthquake waveforms of another earthquake.

Text S1.

In Figure S1, we show the Cross-Correlation Functions (CCFs) computed without 1-bit normalisation between virtual source 4000 and 200, 300, and 400 receiver channels as well as their corresponding dispersion images. The spatial aliasing lines computed with Equation 2 of the main manuscript explain the different aliasing slopes that appear in the dispersion images.

Text S2.

By selecting local maximum energy points from 1-bit CCF dispersion images, we also potentially select high-energy artefacts caused by spatial aliasing. We reject such points prior to performing the inversion and show an example of the selection process in Figure S2. Only decreasing dispersion points remain after the data selection step.

Text S3.

In Figure S3, we show a dispersion image computed from vertical displacement waveforms excited by a vertical source. Similarly to Figure 6c in main manuscript, the dispersion image is simulated with a Discrete Wave Number method (Bouchon 2003) and using velocity gradient of 1 s^{-1}. Apparent DCs, which are constituted of a succession of osculation points from true DCs, appear in the dispersion images. They converge toward a horizontal asymptote of 1.5 km/s given by the V_P velocity in the top sediment layers. As the energy of the true DCs is high around the osculation points, apparent DCs hold most of the energy and can easily be misinterpreted as true DCs. Mistaking apparent DCs for true DCs could potentially happen when considering measurements from the vertical component of OBS and significantly bias the resulting velocity model.

Text S4.

In Figure S4, we show a comparison between the inverted DCs computed with Equation 4 and 5 of the main manuscript. Equation 4 does not perform well for inverting a large number of selected dispersion points as we converge toward a low velocity gradient medium with a large number of inverted DCs. We therefore use Equation 5 to invert selected dispersion points with a better accuracy.

Text S4.

We show the waveforms of a Japan Meteorological Agency velocity magnitude (M_V) 2.5 earthquake, which occurred on November 28, 2019 at 14:17:32 (UTC) at a depth of 30 km. The epicentre is located 15.5 km south east from the close OBS station to the coast (Figure 1). Clear P- and S-waves can be observed for this earthquake which occurred almost below the cable. Moreover, surface waves are generated in similar regions as for the W_w 3.7 earthquake shown in Figure 10.

REFERENCES

Bouchon, M., 2003. A review of the discrete wavenumber method, *Pure Appl. Geophys.*, **160**(3), 445–465.

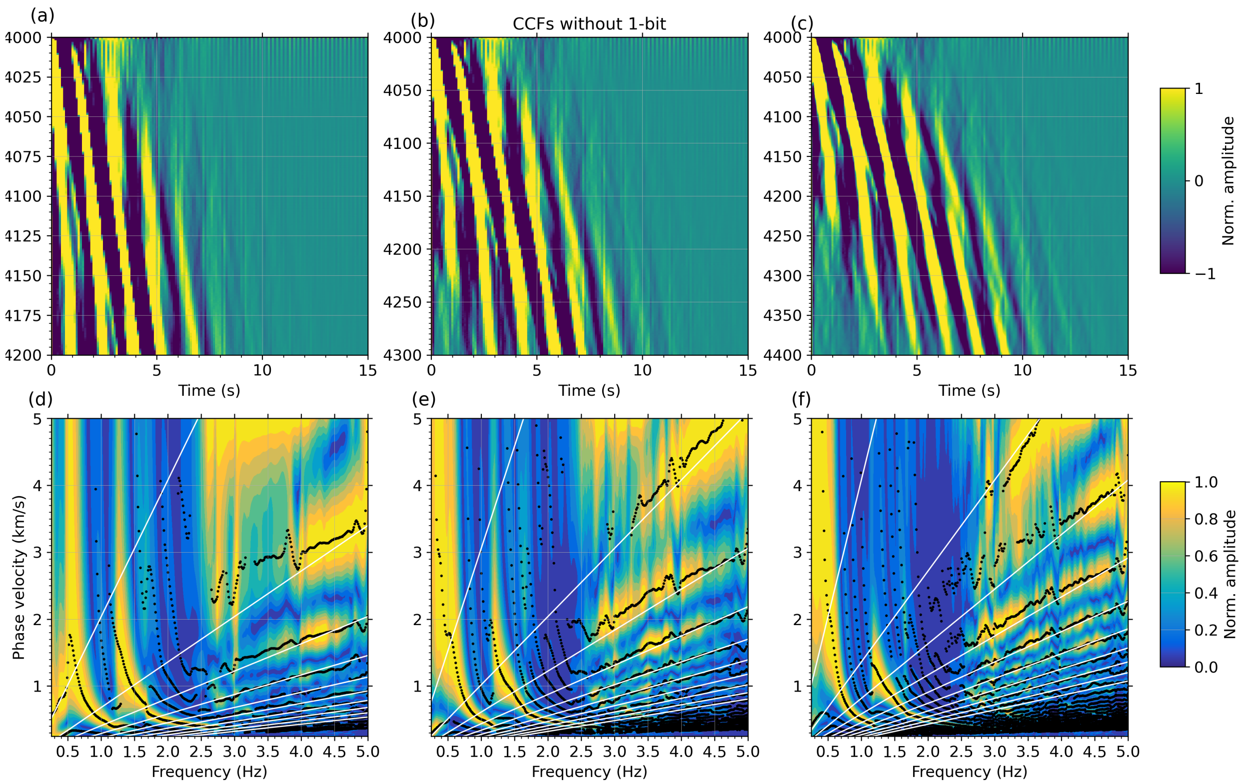

Figure S1. CCFs computed between channel 4000 (virtual source) and (a) 200, (b) 300, (c) 400 receiver channels. The corresponding dispersion images are shown in (d-f). For each panel in (d-f), the spatial aliasing lines computed with Equation 2 of the main manuscript up to $i = 10$ are also shown.

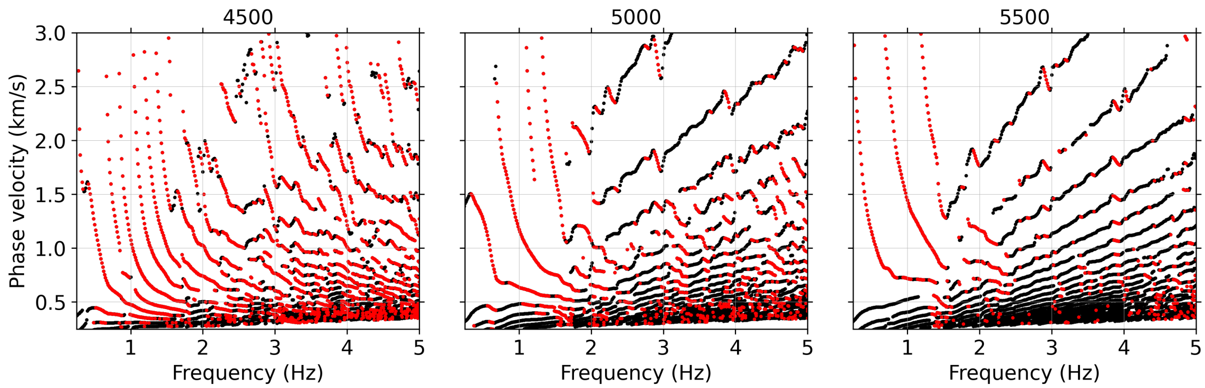

Figure S2. All selected local maxima (black) versus refined selected dispersion points (red) for the dispersion images computed from virtual sources 4500, 5000, and 5500. The dispersion images, which are shown in Figure 5 of the main manuscript, are calculated from 1-bit CCFs and 400 receiver channels.

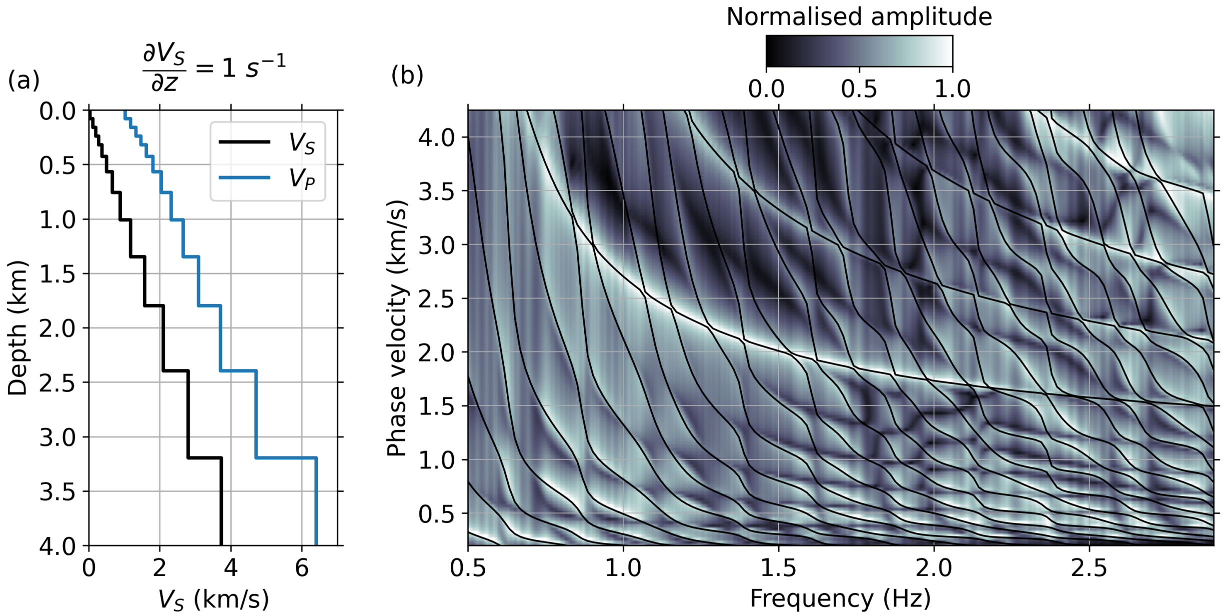

Figure S3. (a) V_S (black) and V_P (blue) velocity profiles for a gradient velocity profile of $\frac{\Delta V_S}{\Delta z}$ $=1\ s^{-1}$. (b) Theoretical dispersion image computed from vertical displacement waveforms generated by a vertical source using the velocity profile shown in (a). The energy of the dispersion image is normalised between 0 and 1 and the theoretical DCs are shown by the black lines.

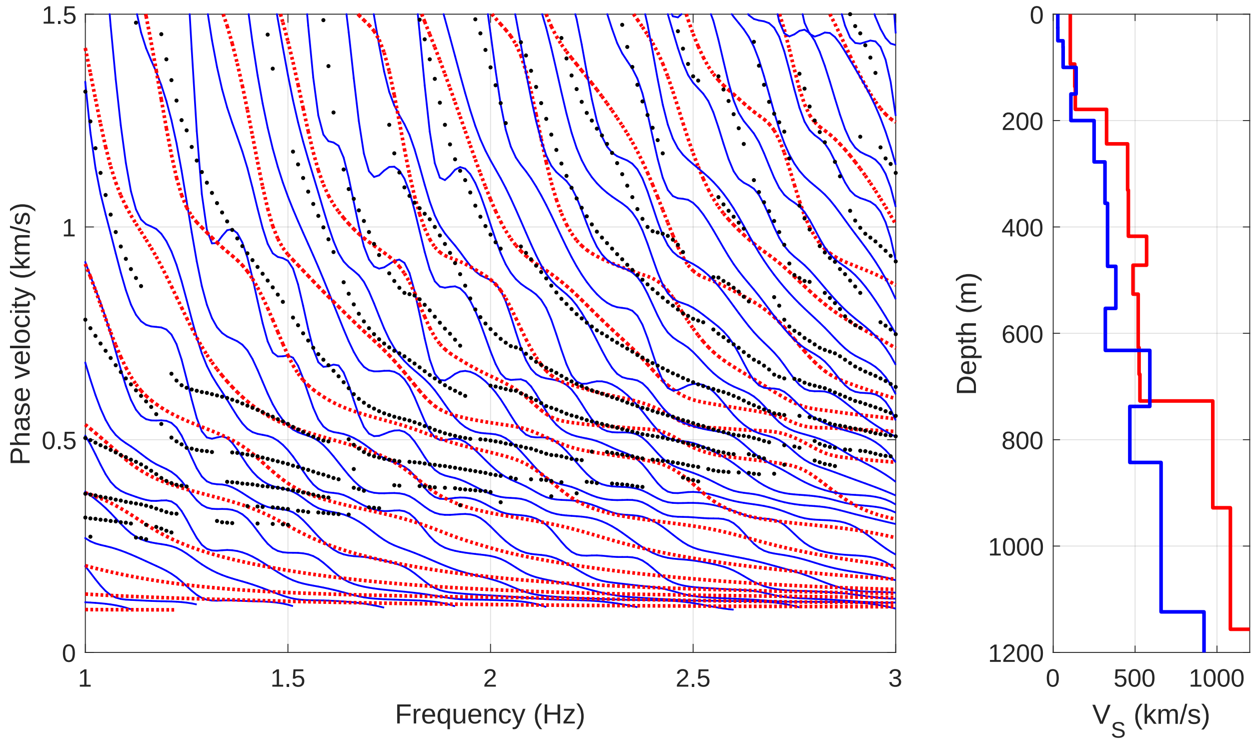

Figure S4. Fitted DCs with Equations (blue) 4 and (red) 5 of the main manuscript and selected dispersion points (black dots) for the dispersion image computed with virtual source 4000. (b) S-wave velocity profiles for the two inversion schemes.

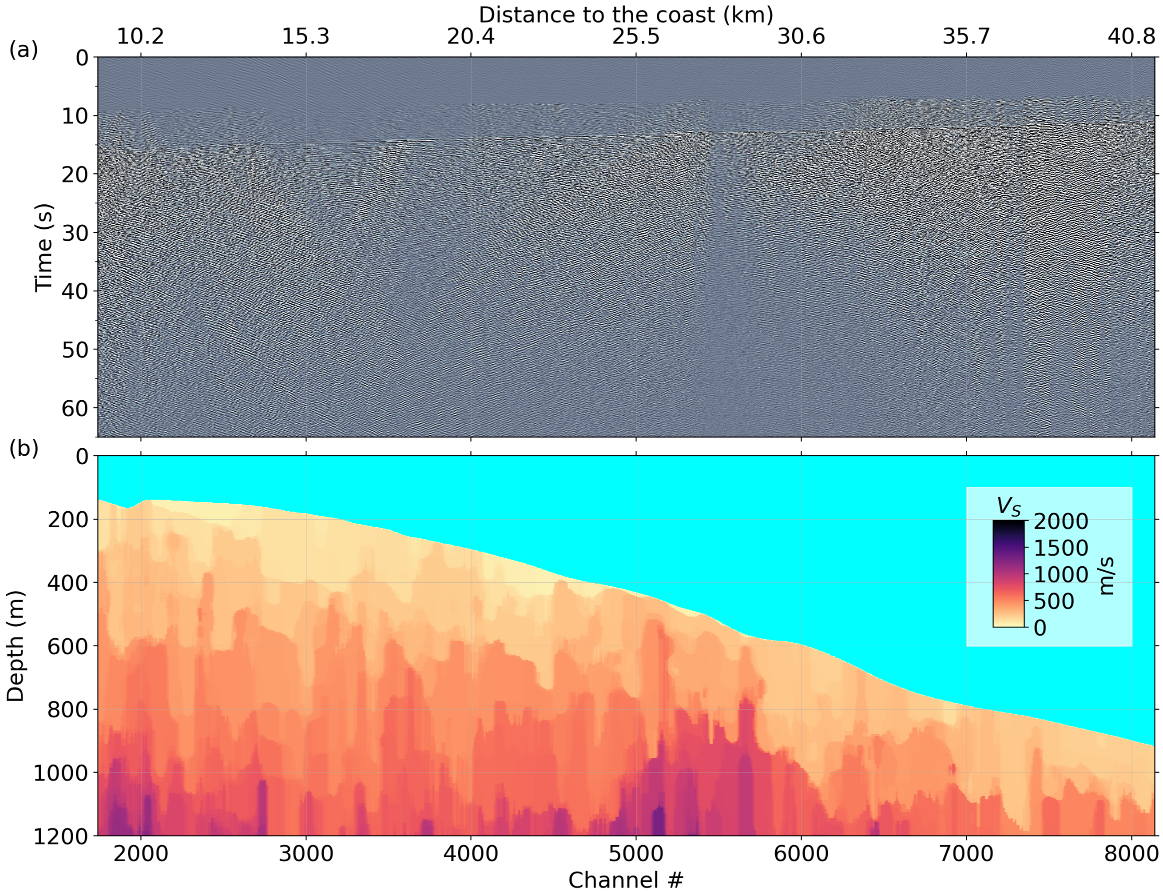

Figure S5. (a) Strain waveforms of a M_V 2.5 earthquake bandpass filtered between 1 and 3 Hz. P- and S-waves arrive around 5 s and 10 s after the origin time, respectively. (b) Zoom on the shallow part of the inverted velocity model.